Materials Science & Engineering C 131 (2021) 112515

Contents lists available at ScienceDirect

Materials Science & Engineering C

journal homepage: www.elsevier.com/locate/msec

Development of bioactive catechol functionalized nanoparticles applicable for 3D bioprinting

María Puertas-Bartolomé [a,b,c], Małgorzata K. Włodarczyk-Biegun [c], Aránzazu del Campo [c,d], Blanca Vázquez-Lasa [a,b,*], Julio San Román [a,b]

[a] Institute of Polymer Science and Technology, ICTP-CSIC, Juan de la Cierva 3, 28006 Madrid, Spain
[b] CIBER's Bioengineering, Biomaterials and Nanomedicine, CIBER-BBN, Health Institute Carlos III, Monforte de Lemos 3-5, 28029 Madrid, Spain
[c] INM – Leibniz Institute for New Materials, Campus D2 2, 66123 Saarbrücken, Germany
[d] Chemistry Department, Saarland University, 66123 Saarbrücken, Germany

ARTICLE INFO

Keywords:
Catechol nanoparticles
Wound healing
3D printing
Cell therapies

ABSTRACT

Efficient wound treatments to target specific events in the healing process of chronic wounds constitute a significant aim in regenerative medicine. In this sense, nanomedicine can offer new opportunities to improve the effectiveness of existing wound therapies. The aim of this study was to develop catechol bearing polymeric nanoparticles (NPs) and to evaluate their potential in the field of wound healing. Thus, NPs wound healing promoting activities, potential for drug encapsulation and controlled release, and further incorporation in a hydrogel bioink formulation to fabricate cell-laden 3D scaffolds are studied. NPs with 2 and 29 M % catechol contents (named NP2 and NP29) were obtained by nanoprecipitation and presented hydrodynamic diameters of 100 and 75 nm respectively. These nanocarriers encapsulated the hydrophobic compound coumarin-6 with 70% encapsulation efficiency values. In cell culture studies, the NPs had a protective effect in RAW 264.7 macrophages against oxidative stress damage induced by radical oxygen species (ROS). They also presented a regulatory effect on the inflammatory response of stimulated macrophages and promoted upregulation of the vascular endothelial growth factor (VEGF) in fibroblasts and endothelial cells. In particular, NP29 were used in a hydrogel bioink formulation using carboxymethyl chitosan and hyaluronic acid as polymeric matrices. Using a reactive mixing bioprinting approach, NP-loaded hydrogel scaffolds with good structural integrity, shape fidelity and homogeneous NPs dispersion, were obtained. The *in vitro* catechol NPs release profile of the printed scaffolds revealed a sustained delivery. The bioprinted scaffolds supported viability and proliferation of encapsulated L929 fibroblasts over 14 days. We envision that the catechol functionalized NPs and resulting bioactive bioink presented in this work offer promising advantages for wound healing applications, as they: 1) support controlled release of bioactive catechol NPs to the wound site; 2) can incorporate additional therapeutic functions by co-encapsulating drugs; 3) can be printed into 3D scaffolds with tailored geometries based on patient requirements.

1. Introduction

Wound healing is a complex process that involves the interaction of different cell types, the presence of bioactive molecules and a matrix scaffold to support regeneration of the damaged tissue. Several disease conditions, such as diabetes, can impair healing and lead to chronic wounds, which are especially difficult to heal, and represent an important global healthcare problem [1–4]. At present, existing wound dressings such as films, hydrogels, foams or wafers can be found to assist the healing process in chronic wounds; and synthetic drugs can be administrated such as silver sulfadiazine to avoid bacterial infection. However, the development of efficient wound dressings to target specific events in the healing process without side effects is still necessary and constitutes a significant target in regenerative medicine [1,5,6].

In this sense, the cutting-edge nanomedicine offers new possibilities to improve the effectiveness of existing wound therapies. For example, incorporation of bioactive and/or drug loaded nanocarriers in wound dressings can provide additional wound healing benefits. Numerous nanocarriers have been used to enhance the drug therapeutic efficacy including liposomes, polymeric, inorganic or lipid nanoparticles (NPs),

* Corresponding author at: Institute of Polymer Science and Technology, ICTP-CSIC, Juan de la Cierva 3, 28006 Madrid, Spain.
E-mail address: bvazquez@ictp.csic.es (B. Vázquez-Lasa).

https://doi.org/10.1016/j.msec.2021.112515
Received 28 June 2021; Received in revised form 19 October 2021; Accepted 22 October 2021
Available online 29 October 2021

nanofibrous structures and nanohydrogels [7–10]. In particular, polymeric NPs have provided good thermodynamic stability, high efficiency as drug carriers, ability to enhance solubilization of hydrophobic drugs and protection against environmental degradation [11–16]. Specially, NPs capacity to provide a localized sustained drug release and subsequently diminish their dose-related toxicity has achieved considerable attention in wound healing therapies [17,18].

Catechols are benzene derivatives with recognized antioxidant and anti-inflammatory activities [19,20]. Our group and others have demonstrated that catechol derived polymers can support healing in chronic wounds by providing successful scavenging of ROS (reactive oxygen species), mitigating the inflammatory response and facilitating the neovascularization [19–24]. Catechol bearing polymeric NPs have attracted much attention as nanocarriers since they can provide sustained drug release while reducing the side effects of several anticancer drugs or antimicrobials [25–27]. Thus, the use of catechol bearing nanocarriers to provide a controlled local drug administration while enhancing the bioactivity of the system can be of great interest for advanced wound healing applications.

Polymeric NPs have been increasingly combined with other biomaterial matrices to obtain hybrid systems with unique physicochemical and biological properties that cannot be accomplished individually. For instance, the integration of antimicrobial loaded polymeric nanoparticles into different hydrogel matrices has shown a great promise to support local treatment of bacterial infections [25,28–30]. The intrinsic properties of hydrogels are favorable for the wound healing process [31–33], however, hydrogel wound dressings are not customizable to fulfil specific conditions [34]. Hydrogel precursors can be processed by 3D bioprinting technology (bioinks) to develop 3D printed scaffolds with tailored geometries based on patient requirements that support cell encapsulation and contribute to enhance wound dressings efficiency [35–39]. Cell therapy has emerged as a promising modality to enhance the wound healing process and restore the damaged tissue by modulating the immune response and promoting angiogenesis [40,41]. Cell loaded 3D bioprinted hydrogel scaffolds of varying porous and multilayered designs are promising constructs to support the proliferation of therapeutic cells. Beyond scaffold design, 3D bioprinting facilitates automation and standardization of the fabrication process, and provide flexibility in the choice of design, materials, therapeutic agents, control over the formulation doses, and release rate can be tailored in response to patient requirements [34,42,43].

The aim of this work is to develop bioactive catechol functionalized polymeric NPs and subsequently design hydrogel bioprinted scaffolds with a controlled NPs release for wound healing purposes. Thus, catechol bearing polymeric NPs with 2 and 29 mol% contents (named NP2 and NP29 respectively) are presented. Their capacity to encapsulate hydrophobic drugs and act as nanocarriers with controlled pharmacokinetic profile is studied along with their antioxidant, anti-inflammatory and neovascularization properties coming from the presence of catechol moieties in their structure. The NP29 are further used as active ingredient in the formulation of an advanced hydrogel bioink using printable mixtures of the polysaccharides carboxymethyl chitosan (CMCh) and hyaluronic acid (HA) loaded with fibroblasts. A reactive 3D bioprinting methodology recently developed by our group is used to fabricate cell-laden NP-3D hydrogel scaffolds with tailorable geometry and particle distribution [44]. The proposed bioprinting approach has several advantages in 3D extrusion bioprinting: (i) *in situ* crosslinking provides appropriate structural integrity to maintain the printed shape, so there is no need for additional crosslinkers that can be cytotoxic; (ii) it avoids postprinting cell seeding, neutralization or washing steps; and (iii) it allows the use of low viscosity starting solutions, which decreases shear stress in encapsulated cells. Finally, the properties of the as-obtained 3D scaffolds are described. The localized NPs release to the wound site is expected to enhance bioactivity by the regulation of the radical oxygen species (ROS) production, control of the constant activation of the inflammatory response, facilitation of the neovascularization, and consequently, cell proliferation and tissue modeling. We expect that this biologically active bioink opens a possibility to engineer 3D scaffolds with enhanced therapeutic performance and potential for the treatment of chronic wounds.

2. Experimental

2.1. Materials

3,4-Dihydroxyhydrocinnamic acid (hydrocaffeic acid, Sigma-Aldrich), thionyl chloride (Scharlau), *N*,*N*-dimethylformamide (DMF) (Scharlau), toluene (Merck), dimethyl sulfoxide (DMSO) (Scharlau), *N*-vinylcaprolactam (Sigma-Aldrich), 1,4-dioxane (Panreac), triethylamine (Scharlau), ethanol (VWR Chemicals), carboxymethyl chitosan (Chitoscience, 85–90% degree of deacetylation, viscosity = 5–300 mPas), sodium hyaluronan (HA) ($M_w \sim 1.5–1.8 \times 10^6$ Da, Sigma Aldrich,), sodium periodate ($NaIO_4$) (Alfa Aesar), ethylene glycol (Sigma), hydroxylamine (Sigma-Aldrich), iron chloride (III) (Sigma-Aldrich), phosphate buffered saline solution (PBS) (10 mM pH 7.4, Gibco), esterase from porcine liver (Sigma-Aldrich), acetone (Scharlau), coumarin-6 (Sigma-Aldrich), and tween 80 (Fluka), were used as received. 2-Hydroxyethyl methacrylate (Sigma-Aldrich) was previously purified according to the literature [45]. Azobisisobutyronitrile (AIBN) (Sigma-Aldrich) was crystallized in methanol (Sigma-Aldrich) prior to use. Oxidized sodium hyaluronan (HAox) was prepared as reported elsewhere [46], with a final oxidation degree of 48 ± 3.2% [47].

2.2. Preparation of catechol bearing NPs

Catechol containing terpolymers were obtained by conjugation of the chloride derivative of hydrocaffeic acid to copolymers of *N*-vinylcaprolactam and 2-hydroxyethyl methacrylate following a previously described protocol [19]. Terpolymers with catechol molar fractions of 2 and 29% (Fig. 1a) were obtained, as quantified by UV spectroscopy (Fig. S1). These catechol derivatized terpolymers will be designated as T2 and T29 respectively regarding their catechol composition. Catechol functionalized NPs were obtained by self-assembly of the amphiphilic T2 and T29 by nanoprecipitation. Briefly, the terpolymer was dissolved in ethanol/acetone 1:1 at 5 mg/mL and the solution was added dropwise into 0.003 M NaCl aqueous solution under continuous stirring, without addition of surfactant. The mixture was stirred at r.t. for 24 h in order to remove the organic solvent and the final NPs concentration was 1 mg/mL. NPs suspensions were sterilized by filtration through 0.22 μM poly (ether sulfone) membranes (PES, Millipore Express, Millex GP) and stored at 4 °C until used. The NPs are designated by the catechol composition as NP2 and NP29 in the following sections.

NPs were loaded with the model drug coumarin-6 (C6) during the nanoprecipitation. Briefly, the terpolymer and C6 were dissolved in ethanol/acetone 1:1 (5 mg/mL polymer and 2 wt-% C6 with respect to the polymer content) and the solution was added dropwise into 0.003 M NaCl aqueous solution under continuous stirring. The mixture was stirred at r.t. for 24 h. NPs suspensions were sterilized by filtration through 0.22 μM PES membranes and stored at 4 °C until used. These loaded NPs are designated as C6NP2 and C6NP29 (for NP2 and NP29, respectively).

2.3. NPs characterization

2.3.1. Particle size distribution and zeta potential

The particle size distribution and zeta potential (ξ) of the NPs were determined by Dynamic Light Scattering (DLS) and laser Doppler electrophoresis (LDE) respectively, using a Malvern Nanosizer NanoZS Instrument at r.t. NPs suspensions at 1 mg/mL were used. The statistical average and standard deviation of mean hydrodynamic diameter (D_h) and particle dispersion index (PDI) were calculated from 6 measurements of 11 runs, while the zeta statistical average and standard

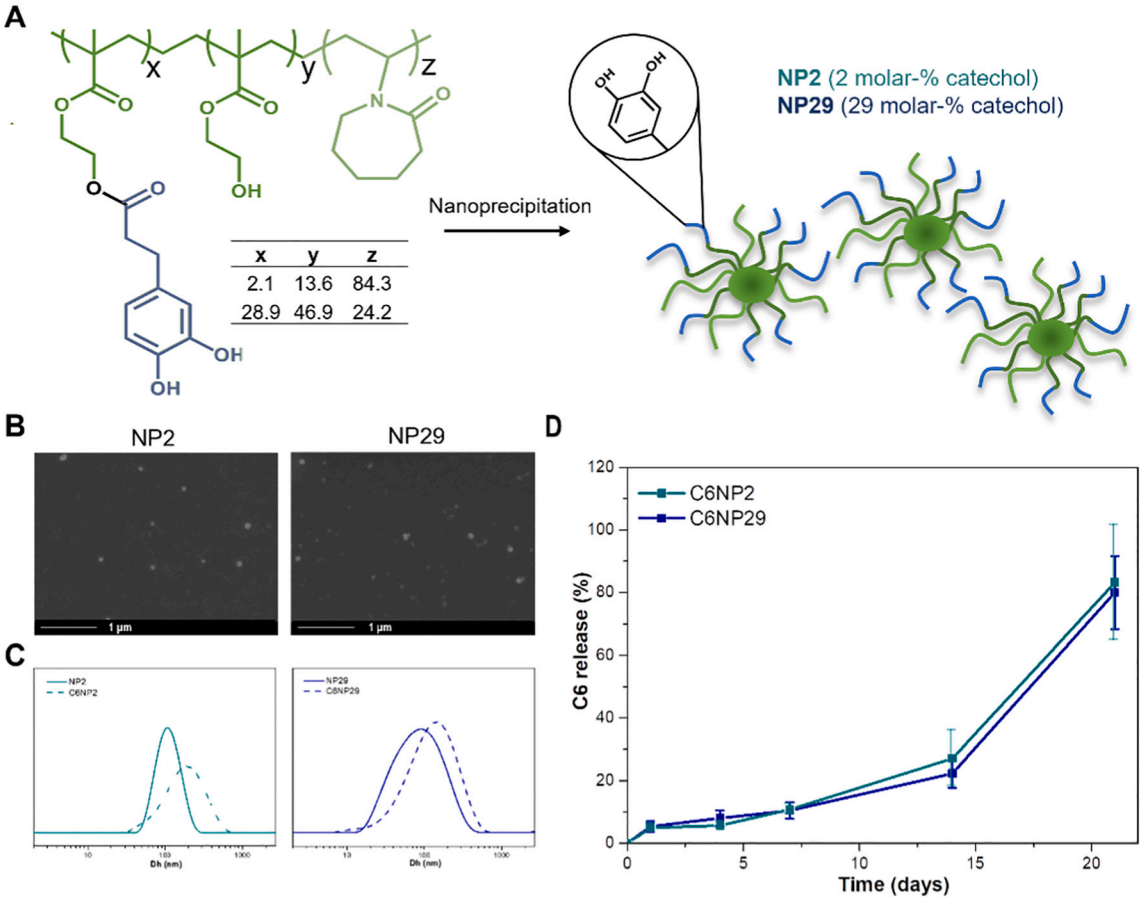

Fig. 1. (A) Scheme of NPs preparation on the basis on T2 and T29 amphiphilic catechol functionalized terpolymers. (B) SEM images of NP2 and NP29. (C) Graph of the particle size distribution of NPs and the C6-loaded NPs obtained by DLS. (D) C6 esterase mediated cumulative release from C6NP2 and C6NP29.

deviation were calculated from 6 measurements of 20 runs each. The morphology of the nanostructures was characterized by Scanning Electron Microscopy (SEM) using a Hitachi SU8000 TED, cold-emission FE-SEM microscope (accelerating voltage 2 kV) at 0.02 mg/mL concentration. The stability of aqueous NPs suspensions was studied by storing them at 4 °C and characterizing the D_h, PDI and ξ at different time points: 1 day, 1 week and 3 weeks.

2.3.2. C6 encapsulation efficiency and release

To calculate the encapsulation efficiency (EE) of C6 in the C6NP2 or C6NP29, water suspensions of NPs were freeze-dried and NPs dissolved in ethanol/acetone 1:1 mixture for 12 h. Samples were analyzed by UV at 450 nm using a NanoDrop One spectrophotometer (Thermo Scientific, Spain). A calibration curve of C6 in ethanol/acetone 1:1 was measured, from which the absorbance of the corresponding non-loaded NPs suspension was subtracted. EE was calculated as the percentage ratio between C6 concentration detected experimentally and the initial C6 concentration added during the nanoprecipitation. A minimum of three replicates were performed, and results given as mean ± SD.

Esterase-mediated release kinetic of C6 from the NPs was analyzed by adding 15 u/mL esterase to 4 mL of C6NP2 or C6NP29 water suspensions and dialyzing (membrane molecular weight cutoff, 3.5 kDa) against 15 mL of 0.5% Tween 80 aqueous solution at 37 °C. At different time points (1, 4, 7, 14 and 21 days), 1 mL of the dialyzing medium was withdrawn and replenished by fresh medium. The absorbance of samples was analyzed by UV at 450 nm using NanoDrop One spectrophotometer. C6 release was calculated by interpolation in the calibration curve of C6 in the same solvent (0.5% tween 80 aqueous solution) after subtraction of the absorbance corresponding to NP2 or NP29. Release data were calculated as the percentage ratio of C6 concentration detected experimentally and the one loaded in the NPs. A minimum of three replicates of each composition were analyzed and results given as mean ± SD.

2.4. NPs biological evaluation

2.4.1. Cell culture

Human dermal fibroblasts (HDF, Innoprot), murine RAW 264.7 macrophages (ECACC, Sigma) and human umbilical vein endothelial cells (HUVEC, Innoprot) were used. HDF and RAW cells were cultured in Dulbecco's modified Eagle's medium (DMEM) supplemented with 4-(2-hydroxyethyl)-1-piperazineethanesulfonic acid (HEPES) for HDF cells or sodium pyruvate (110 mg/L) for RAW 264.7 cells; 10% fetal bovine serum (FBS), 100 units/mL penicillin, 100 µg/mL streptomycin and 200 mM L-glutamine. Endothelial cells were cultured in endothelial cell medium (ECM, Innoprot) supplemented with 5% FBS, 1% endothelial cell growth supplement and 1% penicillin/streptomycin solution. Incubation was carried out at 37 °C, 95% humidity and 5% CO_2. The culture medium was changed every two days.

2.4.2. NPs cytotoxicity

Cell viability was analyzed in the presence of different concentrations of NP2 and NP29. RAW 264.7 cells were seeded in a 96 well-plate at 2.5×10^5 cells/mL density and incubated overnight. The medium was replaced by the corresponding NPs solution (1:1 NPs suspension/DMEM to give final particle concentrations from 0.0156 to 0.5 mg/mL). After 24 h of culture, cell viability was determined by Alamar Blue staining assay (Sigma-Aldrich) by measuring fluorescence at (Ex 530–560 nm/

Em 590 nm) using a Multi-Detection Microplate Reader Synergy HT (BioTek Instruments; Vermont, USA). A minimum of 6 replicates was analyzed for each composition. Results were normalized to the control (cells seeded without NPs) and expressed as a mean percentage of relative cell viability ± SD. Analysis of variance (ANOVA) using Tukey grouping method of the results for loaded and non-loaded NPs, and for NP2 and NP29 compositions at the concentrations from 0.0156 to 0.25 mg/mL was performed at a significant level of $*p < 0.05$.

2.4.3. Cell uptake of C6-loaded NPs

Murine RAW 264.7 macrophages (ECACC, Sigma) were selected to investigate endocytosis of C6NP2 and C6NP29 systems. RAW 264.7 cells were seeded into a 96 well-plate at the density of 1×10^5 cells/mL in complete DMEM and incubated overnight. Afterward, the medium was replaced by the corresponding NPs solution 1:1 NPs suspension/DMEM to give final particle concentrations in the range of 0.0156 to 0.25 mg/mL and incubated for 24 h. Then, cells were washed with PBS and fixed with paraformaldehyde solution in PBS (3.7 w/v %). Nuclei were stained with DAPI (Thermofisher) and fluorescence images were taken at 60× magnification using a microscope Nikon Eclipse TE2000-S with camera NikonDS-Ri2.

2.4.4. NPs antioxidant activity

Antioxidant properties of NP2 and NP29 were evaluated. For that, ROS quantification of RAW 264.7 macrophages in the presence of NP2 and NP29 at different concentrations was carried out using 2′,7′-dichlorofluorescin diacetate (DCFH-DA), a nonfluorescent compound that becomes DCF (2′,7′-dichlorofluorescein) and emits fluorescence after being oxidized. RAW 264.7 were seeded at 2.5×10^5 cells/mL density and incubated for 24 h in complete medium. The medium was removed and replaced by the corresponding NPs solution 1:1 NPs suspension/DMEM to give final particle concentrations in the range of 0.0156 to 0.25 mg/mL. After 24 h of culture, cells were washed 3 times with PBS and 100 μL of a 40 mM DCFH-DA in PBS were added to the cells. Cells were incubated at 37 °C for 30 min and washed with PBS another 3 times. Then, 100 μL of H_2O_2 solution in PBS (100 mM) were added to the wells. Well-plate was incubated for 15 min and fluorescence was measured at 485 nm excitation/580 nm emission with a UV multiplate reader (Biotek Synergy HT, Winooski, VT, USA). Analysis of variance (ANOVA) using Tukey grouping method of the results for NP2 and NP29 treated-cells was performed in comparison with the positive control of cells treated with H_2O_2 at significant levels of $*p < 0.05$, $**p < 0.01$ and $***p < 0.001$.

2.4.5. NPs anti-inflammatory behavior

The anti-inflammatory activity of NP2 and NP29 nanoparticles was evaluated using the nitric oxide (NO) inhibitory assay [48]. RAW 264.7 cells were seeded in 96-well plates at a density of 2.5×10^5 cells/mL and incubated at 37 °C for 24 h. Afterward, the medium was removed and replaced by the corresponding NPs solution 1:1 NPs suspension/DMEM to give final particle concentrations in the range 0.0156 to 0.25 mg/mL. After 24 h of culture, medium was removed again and 5 μg/mL of lipopolysaccharides from *E. coli* 055:B5 (LPS, Sigma) were added to half of the samples. These samples were incubated for next 24 h, either with or without LPS. NO concentration was determined by the Griess reaction [49,50]. Aliquots (100 μL) of supernatants were mixed with the Griess reagent (Sigma-Aldrich) (100 μL) and after 10 min, absorbance at 548 nm was measured. A minimum of 6 replicates was analyzed and data were expressed as the percentage of NO production and cell viability and given as mean ± SD. Analysis of variance (ANOVA) using Tukey grouping method of the results for NP2 and NP29 treated-cells was performed in comparison with the positive control of cells treated with LPS at significant levels of $*p < 0.05$, $**p < 0.01$ and $***p < 0.001$. Cell viability of RAW 264.7 cells in the presence of LPS and the different concentrations of NP2 and NP29 was evaluated in parallel by Alamar Blue staining assay as previously explained in this section.

2.4.6. VEGF production quantification

HDF were seeded into 12-well plates at 100,000 cells/mL. Cells were treated with serum-free medium for 2 h. Then, they were exposed to different concentrations of NP2 and NP29 prepared in serum-free medium (0.25, 0.125 and 0.0625 mg/mL) for 48 h. Then, medium supernatants were centrifuged for 1 min at 1400 r.p.m. and VEGF release was evaluated by ELISA experiment according to the manufacturer's instructions (VEGF Human ELISA Kit, Invitrogen, Thermo Scientific). The cell viability was determined using trypsin and a cell counter (Innoprot) and results were normalized to 10^6 cells. Cells without NPs treatment were used as control. Analysis of variance (ANOVA) using Tukey grouping method of the results for NP2 and NP29 treated-cells was performed in comparison with the cells control at significant levels of $*p < 0.05$, $**p < 0.01$ and $***p < 0.001$.

VEGF release by endothelial cell lines seeded on the top of NPs loaded hydrogels was also evaluated. Hydrogels containing 1 mg/mL NP29, 2 wt-% CMCh, 4 wt-% HAox and 0.4 wt-% HA (denoted as CMChNP29/HAox-HA) were directly prepared in 12-well plates right before seeding. Hydrogels without NPs (denoted as CMCh/HAox-HA) were used as control. Endothelial cells in serum free medium were seeded on the top of the hydrogels at 300,000 cells/mL. After 48 h of culture, medium supernatants were centrifuged for 1 min at 1400 r.p.m. and VEGF release was evaluated by ELISA experiment according to the manufacturer's instructions. DNA content was analyzed by Picogreen assay of cells within the gels and results were normalized to 10^6 pg DNA. Analysis of variance (ANOVA) using Tukey grouping method of the results for CMChNP29/HAox-HA sample was performed in comparison with CMCh/HAox-HA sample at significant levels of $*p < 0.05$, $**p < 0.01$ and $***p < 0.001$.

2.5. NP-hydrogel inks formulation and 3D printing

A two-component ink containing NP29 was formulated and named CMChNP29/HAox-HA. Solution A contained 1 mg/mL NP29 suspension and 2 wt-% CMCh solution in PBS (pH = 7.4). Solution B contained 4 wt-% HAox and 0.4 wt-% HA in 0.1 M NaCl. For cell-laden scaffolds, L929 fibroblasts (ATCC, Germany) were suspended in the bioink precursor solution A prepared in RPMI 1640 (Gibco) (instead of PBS). A cell concentration of 1×10^6 cells/mL was used. Bioink formulation without NPs (further denoted as CMCh/HAox-HA) was used as control.

3D scaffolds were fabricated using a 3D Discovery printer (RegenHu, Switzerland) modified to adapt a static mixing tool (RegenHu, Switzerland) following a printing methodology previously described by our group [44]. Briefly, two 1 mL syringes (RegenHu, Switzerland) were loaded with the hydrogel precursors solutions A and B. They were simultaneously extruded by mechanical printer motor into the static mixing tool in a 1:1 volume ratio, where they were mixed and immediately began to crosslink. Finally, the crosslinked hydrogel was extruded through the needle giving a final NP29 concentration of 0.25 mg/mL.

A grid square design (12 × 12 mm, 1.5 mm interstrand distance) was used to fabricate two-layer scaffolds. Same architecture was used for all the experiments performed in this work. One sacrificial 4 cm line was printed before the scaffold for material homogenization in the static mixer. Scaffolds were printed onto glass cover slips using a print head movement speed of 15 mm/s and a plunger speed of 0.06 mm/s (residence time of around 2.5 min), both processes were controlled by the software modified by RegenHu. A conical polyethylene needle with an inner diameter of 200 μm was used. A cytocompatible post-printing stabilization step was carried out by immersion of the printed scaffolds in a 20 mM $FeCl_3$ aqueous solution for 7 min [44].

2.6. Characterization of the inks and the printed scaffolds

2.6.1. Rheological characterization

Rheological measurements of the inks were performed using a

rotational rheometer (ARG2, TA Instruments). A parallel plate geometry was used, with sand-blasted plates of 25 mm diameter. Measurements were performed at 25 °C. A solution volume of 150 μL was used for each measurement, and measuring gap was predefined at 300 μm. Inks with and without NPs were analyzed. All experiments were performed at least in triplicate.

The shear (G′) and loss modulus (G″) were recorded in time sweep experiments during 5 min at 1 Hz and 1% oscillatory strain. 75 μL of the solution A (with or without NPs) was deposited on the lower plate of the rheometer, followed by deposition of 75 μL of the solution B on the top. Solutions were quickly mixed by pipetting and compressed between the measuring plates. The gelation time, defined at the crossover point of G′ and G″, was extracted from the rheology curves. Each sample was measured three times and the average gelation time value calculated. Frequency sweep (1–300 Hz) experiments at 1% strain were performed for CMChNP29/HAox-HA and CMCh/HAox-HA hydrogels. The viscosity of the hydrogels was also determined in a rotational flow sweep experiment at increasing shear rates from 0.2 to 500 1/s right after hydrogel formation.

2.6.2. Morphological evaluation of 3D printed scaffolds

The printed scaffolds were inspected and imaged with an optical microscope (Nikon SMZ800N, Germany) and camera (Samsung 13MPx). The surface morphology was analyzed with Multimode AFM (Veeco Instruments).

2.6.3. In vitro stability of the printed scaffolds

In vitro swelling and degradation assays were performed in physiological conditions (PBS pH = 7.4 at 37 °C) for CMChNP29/HAox-HA and CMCh/HAox-HA printed scaffolds. For swelling experiments, freshly printed two-layers scaffolds were weighed (W_d) and incubated in 3 mL of PBS for 0.5, 1, 4 and 18 h. At each time point, scaffolds were removed from PBS, carefully dried with tissue paper, and weighed again (W_t). The water uptake was calculated using the following equation:

$$\text{Water uptake } (\%) = [(W_t – W_d)/W_d] \times 100$$

For degradation analysis, scaffolds were dried at 60 °C, weighed (W_0) and incubated in PBS for different times (1, 4, 7, 14 and 28 days). At the specific time points scaffolds were washed with distilled water, dried at 60 °C, and weighed again (W_t). Weight loss was calculated at each time gravimetrically and weight remaining of the samples was defined as following equation:

$$\text{Weight remaining } (\%) = [1 – (W_0 – W_t)/W_0] \times 100$$

A minimum of four replicates of each sample was analyzed for the experiments and results given as mean ± SD. Surface morphology of printed scaffolds after incubation in PBS for 1 to 28 days was qualitatively analyzed by optical microscope Nikon Eclipse TE2000-S with camera NikonDS-Ri2 (Nikon SMZ800N, Germany).

2.6.4. In vitro NPs release kinetics from the printed scaffolds

The release of NP29 nanoparticles from the two-layer printed scaffolds was evaluated. The release of NP29 from solvent-casted hydrogel films with the same composition was also measured for comparison purposes. Freshly printed scaffolds (or casted films) were immersed into 3 mL of PBS pH 7.4 and stored at 37 °C. At different time points (1, 4, 7 and 14 days), catechol NPs concentration was quantified by measuring the absorbance of the PBS at the maximum absorbance wavelength of the catechol (280 nm) using a NanoDrop One (Thermo Fisher Scientific). A calibration curve of hydrocaffeic acid in PBS was used, and the cumulative release percentage was calculated for each sample. A minimum of 4 replicates was analyzed for each time point and results given as mean ± SD.

2.7. Biological evaluation of bioprinted scaffolds

2.7.1. Cell cultures

L929 Fibroblasts were cultured in RPMI 1640 phenol red free medium (Gibco, 61870-010) supplemented with 20% fetal bovine serum (FBS, Gibco, 10270), 200 mM L-glutamine and 1% penicillin/streptomycin (Invitrogen). Incubation was carried out at 37 °C, 95% humidity and 5% CO_2. The culture medium was changed every two days.

2.7.2. Live dead assay of bioprinted scaffolds

Cell viability of L929 fibroblasts within the NP-loaded hydrogel scaffolds was evaluated after bioprinting using fluorescein diacetate (FDA, Sigma-Aldrich) and propidium iodide (PI, Sigma Aldrich) stainings to detect live and dead cells, respectively. L929 fibroblasts encapsulated in bulk hydrogel (no printing) after 1 day of culture were used as control. Stabilization step with Fe^{3+} (explained in Section 2.5) was performed for both printed and non-printed formulations. At different time points of culture (1, 4, 7 and 14 days) scaffolds were washed with PBS and incubated with FDA (20 μg/mL) and PI (6 μg/mL) for 10 min at r.t. Samples were washed 3 times with PBS and fluorescence images were taken with Nikon Ti-Ecllipse microscope (Nikon Instruments Europe B.V., Germany). To calculate the percentage of viable cells, live and dead cells were quantified in a minimum of 5 images for 3 independent samples using the Image-J software. Analysis of variance (ANOVA) using Tukey grouping method of the results for printed scaffolds at different time points, was performed in comparison with the non-printed sample at significant levels of $*p < 0.05$, $**p < 0.01$ and $***p < 0.001$.

2.7.3. Immunostaining of bioprinted scaffolds

Immunostaining of the printed scaffolds was carried out at different times of culture (1, 4, 7 and 14 days). At each specific time point, cells were fixed with PFA 3.7% *w/v* for 15 min, permeabilized with 0.5% Triton-X 100 in PBS for 15 min and blocked with 0.1% Triton-X 100 and 5% w/v BSA (PBST solution) for 20 min. Scaffolds were incubated in 1:1000 vinculin rabbit antibody (Thermofisher) for cytoskeleton labeling and 1:200 Alexa fluor-546 Phalloidin (Thermofisher) for focal adhesion staining in PBST at r.t. for 1 h. Samples were rinsed 3 times with PBST and incubated with secondary antibody Alexa flour-488 goat antirabbit (Thermofisher, 1:500 dilution) to stain cytoskeleton. They were rinsed twice with PBST, incubated with 1:1000 DAPI (Thermofisher) in PBS for 20 min for nuclei staining, and rinsed twice in PBS. Finally, fluorescence imaging was carried out using a Zeiss LSM 880 confocal microscope, and fluorescence images of nuclei staining with DAPI were taken at 2× magnification using a microscope Nikon Eclipse TE2000-S with camera NikonDS-Ri2.

2.7.4. Alamar Blue staining assay of bioprinted scaffolds

Alamar Blue staining assay was carried out to quantify cell proliferation of L929 fibroblasts within the printed scaffolds over a 14-days period by measuring fluorescence at Ex 530–560 nm/Em 590 nm using a Multi-Detection Microplate Reader Synergy HT (BioTek Instruments; Vermont, USA). A minimum of 6 replicates of 4 independent samples was analyzed for each scaffold composition. Results were normalized to the control (hydrogel without NPs after 1 day of culture) and expressed as the mean percentage of relative cell viability ± SD. Analysis of variance (ANOVA) using Tukey grouping method of the results for CMChNP29/HAox-HA sample was performed in comparison with the CMCh/HAox-HA control sample at significant levels of $*p < 0.05$, $**p < 0.01$ and $***p < 0.001$.

3. Results and discussion

3.1. Preparation and characterization of catechol NPs

Amphiphilic terpolymers were obtained by free radical

copolymerization of an acrylic and a vinyl monomer, and the subsequent post-synthesis conjugation with hydrocaffeic acid to introduce long-arm catechol side groups in the polymer chain [19]. Terpolymers with different catechol compositions, *i.e.* 2 and 29 M %, were obtained and used in this study. The different reactivity ratios of the monomers *N*-vinylcaprolactam and 2-hydroxyethyl methacrylate (previously studied by Jansen et al.) [51] lead to the formation of copolymers with a gradient distribution of monomeric sequences [20]. This architecture along with the conjugation of the catechol side groups provided terpolymers with an appropriate hydrophilic/hydrophobic balance to self-assemble into core-shell nanoparticles in aqueous media (Fig. 1A). Spherical and monodispersed nanoparticles were imaged by SEM (Fig. 1B) giving mean particle sizes of 81.3 ± 0.8 nm for NP2 and 69.0 ± 1.0 nm for NP29. DLS analysis of NPs aqueous suspensions revealed narrow, unimodal size distributions (Fig. 1C) with mean hydrodynamic diameters (D_h) of 109 ± 6.6 nm for NP2 and 72 ± 8.7 nm for NP29 (swollen) and low PDI values (Table 1), indicating that homogeneous populations were obtained. The particle sizes obtained by DLS differed from those observed by SEM. This can be explained by the fact that SEM measurements were performed for NPs in the dry state, whereas DLS provided the hydrodynamic diameter of NPs in water. Zeta potential values of −20.8 ± 2.1 and − 24.9 ± 1.1 mV were obtained for NP2 and NP29 respectively (Table 1), which were negative enough to ensure stability. The difference in the negative surface charge of the NPs suggests the catechol groups are located at the surface of the NPs. The exposure of the catechol groups is expected to positively contribute to the beneficial bioactive properties of the NPs [21,52,53]. Aqueous dispersions of NP2 were stable in the medium until 3 weeks of storage at 4 °C, as depicted by the relatively low increase in the D_h and zeta potential values during storage time (Table S1). However, NP29 showed macroscopic aggregates after 3 weeks. This fact can be probably due to an "auto-oxidation" process of the catechol groups located at the surface, as previously explored by other groups [54,55].

The capability of the NPs to entrap hydrophobic compounds was tested using coumarin-6, frequently used as a model hydrophobic drug and a fluorescent tracer to study the cellular uptake of loaded NPs [56]. C6 was added to the solution during nanoprecipitation. The amount of C6 loaded and the release profile of the C6-loaded NPs (C6NP) were evaluated. C6 encapsulation into the core during the self-assembly process was successful and EE values were around 70% for both NPs compositions (Fig. 1C and Table 1). It can be observed that C6 loading caused a slight increase in the diameter of the NPs. C6 release from the NPs was studied *in vitro* by an esterase-mediated dialysis method. The release kinetics (Fig. 1D) showed sustained release with zero order kinetics during the first 14 days and exponential release for longer periods. An initial sustained release is a very important feature for drug delivery, as a premature release can result in dangerous side effects and low effectiveness of the therapy [57]. We conclude that NP2 and NP29 could act as nano-vehicles to carry hydrophobic drugs that can be cytotoxic when administered systemically (not locally), such as curcumin [58], melatonin [59], amphotericin B [9] and other anti-inflammatory or antimicrobial drugs, beneficial for the treatment of skin injures [60].

Table 1
Mean hydrodynamic diameter (D_h), polydispersity index (PDI) and zeta potential (ξ) of nude and C6-loaded NPs, along with C6 encapsulation efficiency (EE) values.

Sample	D_h (nm)	PDI	ξ (mV)	EE (%)
NP2	109 ± 6.6	0.07 ± 0.02	−20.8 ± 2.1	–
C6NP2	153 ± 2.9	0.27 ± 0.04	–	66.1 ± 2.9
NP29	72 ± 8.7	0.42 ± 0.07	−24.9 ± 1.1	–
C6NP29	107 ± 2.2	0.42 ± 0.06	–	74.5 ± 7.0

3.2. Biological behavior of catechol NPs

Bioactive properties of the catechol functionalized NPs of potential relevance for wound care management were evaluated in *in-vitro* studies. RAW 264.7 macrophage cell line was chosen, since macrophages have a key role in the regulation of the inflammatory reaction of chronic wounds [61]. Fluorescent C6 is used to trace the cellular uptake of the C6NPs by RAW264.7 macrophages. Fig. 2A shows images of the cells exposed to different concentrations of C6NPs after 24 h of culture. Green fluorescent NPs of both compositions (C6NP2 and C6NP29) were observed inside the cells. NPs uptake by the cells was observed already at the lowest NPs concentration (0.0156 mg/mL). These results corroborate that NP2 and NP29 are internalized by cells, presumably by endocytosis process according to their size [62]. The cytotoxicity of C6-loaded and non-loaded NPs was also tested using macrophages line (Fig. 2B). High cell viability was observed at NPs concentrations <0.5 mg/mL but it decreased to 70% for the highest tested concentration (0.5 mg/mL) after 24 h of incubation. However, no significant differences were noticed comparing loaded and non-loaded NP, neither NP2 and NP29 compositions within the concentration range 0.0156–0.25 mg/mL.

A cellular based assay was carried out to evaluate the antioxidant properties of the catechol NPs [63–66], more specifically their capacity to reduce intracellular ROS production of macrophages previously subjected to oxidative stress with H_2O_2. Fig. 2C shows that addition of NP2 and NP29 to the cell culture at concentrations 0.125–0.25 mg/mL significantly decreased ROS production (compared to H_2O_2 treated macrophages without NPs). This reduction was more prominent in NP29 treated samples, which were able to moderate ROS production at 0.0625 mg/mL concentration. These results confirm that the antioxidant activity of catechol NPs is associated and increases with the catechol content in the terpolymer. ROS are continuously generated by cells as a normal metabolic byproduct [67,68]. In chronic wounds, ROS production generally exceeds the capability of the endogenous antioxidant defense [69–71]. This uncontrolled ROS overproduction induces oxidative stress, severe tissue damage and activates the inflammatory response [5,67,72,73]. Consequently, the wound remains in the inflammatory phase for too long, which hinders tissue regeneration and healing [6,54,74]. At sight of the antioxidant activity of catechol groups, the sustained release of the catechol NPs embedded into a printed scaffold is expected to provide a continuous source of ROS scavenger to the wound, beneficial for the wound healing process.

To assess the anti-inflammatory activity of the catechol NPs, the NO inhibitory assay was used. NO acts as an intermediary and regulator agent in inflammatory reactions [48,75]. NO reduction by the materials indicates their anti-inflammatory properties. The ability of uptaken NPs to inhibit NO production of macrophages exposed to the pro-inflammatory agent LPS was evaluated. NO production of LPS-treated macrophages with different cytocompatible concentrations of NPs, as well as the corresponding cell viability values are displayed in Fig. 2D. Both NPs formulations showed a NO inhibition effect in a dose-depended manner. NP2 were able to significantly reduce NO production from 0.25 to 0.0625 mg/mL, compared to the positive control of LPS-treated macrophages without NPs. For NP29 formulation, significant NO inhibition was observed for concentrations from 0.25 to 0.0313 mg/mL. Therefore, NO inhibition of LPS-treated macrophages was more efficient for NP29 formulation, following a similar trend to that of the ROS production. These results indicate that the anti-inflammatory activity of NPs is related to the catechol composition, as previously reported [76–79]. There are two reported strategies through which catechol groups can reduce NO production: (1) by inhibiting the LPS signaling, and (2) by directly quenching the NO [77], which demonstrates the potential of catechol to mitigate inflammatory damage. The anti-inflammatory activity is especially desirable in the treatment of chronic wounds, when the inflammatory stage is too long and inhibits tissue regeneration [6,64,80].

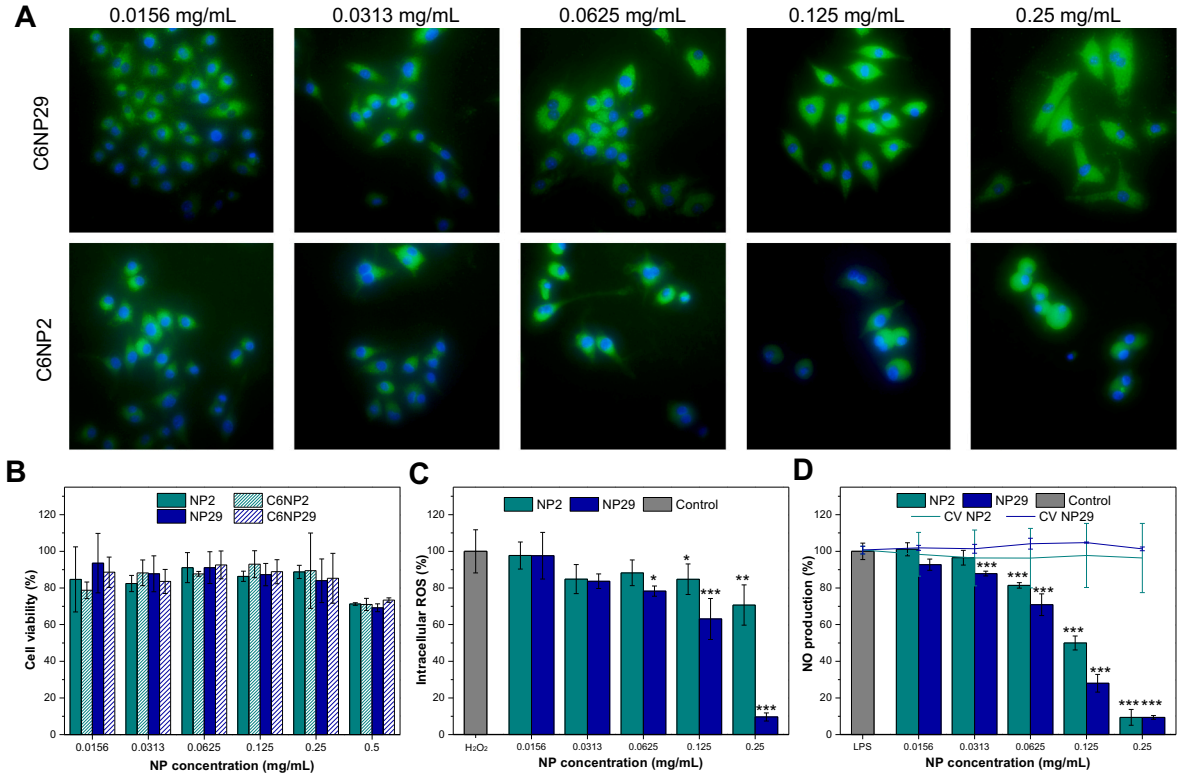

Fig. 2. Biological assay of NPs using RAW 264.7 macrophages: (A) Microscope images of RAW exposed to different concentrations of C6NP2 and C6NP29 for 24 h. (B) Cytotoxicity of C6-loaded and non-loaded NP2 and NP29. ANOVA of the results between loaded and non-loaded NPs for NP2 and NP29 compositions at the concentrations from 0.0156 to 0. 5 mg/mL was performed at a significant level of $*p < 0.05$. (C) ROS production by RAW 264.7 after treatment with H_2O_2 and different concentrations of NP2 and NP29. (D) NO production of LPS-treated RAW 264.7 with different concentrations of NPs, as well as the corresponding cell viability (CV) values. ANOVA of the results for NP2 and NP29 treated-cells was performed in comparison with the positive control (cells treated with H_2O_2 or LPS) at significant levels of $*p < 0.05$, $**p < 0.01$ and $***p < 0.001$.

Angiogenesis or neovascularization plays a key role in regenerative processes. New blood vessel formation provides nutrients and oxygen supply, removes metabolic waste and reduces the risk of infection, essential for the reparation of damaged tissues [81–84]. However, rapid angiogenesis is still a challenge in skin regeneration [83,85]. The neovascularization process is usually induced by growth factors released by cells. Among them, vascular endothelial growth factor (VEGF) is the most potent angiogenic growth factor that plays a critical role in the regulation of wound angiogenesis [86–88]. In this study, the direct effect of catechol nanoparticles on the *in vitro* VEGF expression of cells was examined. VEGF expression of 2D fibroblasts culture exposed to 3 concentrations of NP2 or NP29 was evaluated (Fig. 3A). NP29 at 0.24 mg/mL notably enhanced VEGF expression in fibroblasts. However, VEGF expression of fibroblasts treated with NP2 did not differentiate from the control. To further evaluate the effect of NP29 on the angiogenic process, endothelial cells were seeded on CMCh/HAox-HA and CMChNP29/

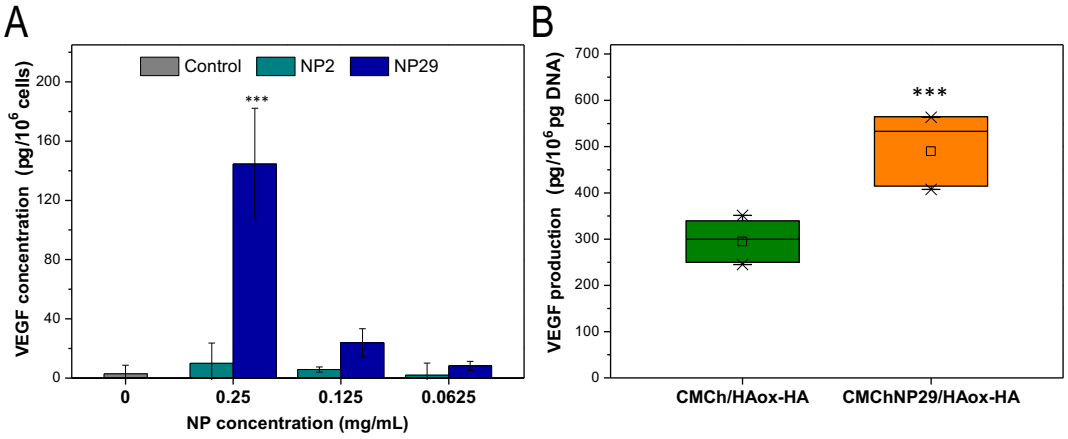

Fig. 3. (A) VEGF expression of 2D fibroblasts culture exposed to different concentrations of NP2 or NP29 and evaluated by ELISA assay. ANOVA of the results for NP2 and NP29 treated-cells was performed in comparison with the cells control at significant levels of $*p < 0.05$, $**p < 0.01$ and $***p < 0.001$. (B) VEGF secretion of endothelial cells seeded on CMCh/HAox-HA and CMChNP29/HAox-HA gels analyzed by ELISA. ANOVA of the results for CMChNP29/HAox-HA sample was performed in comparison with CMCh/HAox-HA sample at significant levels of $*p < 0.05$, $**p < 0.01$ and $***p < 0.001$.

HAox-HA hydrogels as a proof of concept, and VEGF secretion was analyzed by ELISA (Fig. 3B). VEGF production of endothelial cells in the NP-loaded hydrogel was significantly higher respect to the non-loaded hydrogel. These findings corroborate previous studies on the *in vivo* response of catechol containing IPN membranes reported by the authors, where catechol functionalized terpolymer/chitosan/hyaluronic acid hydrogels demonstrated to promote *in vivo* blood vessels formation [21]. They also align with reported observations of other authors that suggest a pro-angiogenic effect of catechol containing polymers. For example, Shin et al. [89] and Park et al. [90] demonstrated the enhanced *in vivo* angiogenesis capacity of stem cells encapsulated in hyaluronic acid derivatives functionalized with catechol groups, for the treatment of ischemic diseases. Also, Xu et al. showed the upregulating capacity of catechol/ε-poly-L-lysine polymers in an *in-vivo* full-thickness cutaneous wound model [91]. Therefore, we envision that catechol NPs integrated into hydrogel scaffolds could support the neovascularization process at the wound site by upregulating the expression of VEGF and, consequently, accelerating the proliferative stage of the healing process.

3.3. 3D bioprinting of NP-loaded hydrogel bioink

The flexibility of 3D bioprinting to produce scaffolds with different material, bioactive and cellular components provides new perspectives for wound healing therapies [43,92–94]. In this sense, we addressed the integration of catechol functionalized NPs into a hydrogel bioink loaded with L929 fibrobasts and the possibility to print 3D scaffolds. NP29 formulation was selected for these studies because of its higher bioactivity observed in the previous section as consequence of its higher catechol content. A previously developed two component bioink based on the natural polysaccharides carboxymethyl chitosan (CMCh) and hyaluronic acid (HA) was used as hydrogel matrix [44]. The carboxymethyl modification makes CMCh soluble at neutral conditions and compatible with cell encapsulation, which avoids neutralization or washing steps commonly used for pure chitosan-based printing [95–97]. NP29 were added to the CMCh solution and an homogeneous dispersion of the NPs in the CMCh was obtained. The second component was a mixture of HA and HAox adequate to achieve similar viscosities of the two reactive components, which is essential for homogeneous mixing during the printing process [98,99]. The aldehyde groups of the HAox form Schiff-bases with the free amine groups of CMCh [46] to form a crosslinked network [21,100–102]. The reversible character of Schiff-bases is beneficial for printing, since dynamic crosslinking is expected to show shear thinning behavior. The final post-printing stabilization step carried out with $FeCl_3$ provides additional crosslinking points to the network through Fe (III) coordination complexes with hyaluronic acid [103], increasing the long-term stability of the scaffold, as previously demonstrated [44].

A dual-syringe system with a static mixing tool was applied for bioprinting, which allows *in situ* crosslinking of the two-reactive components (Fig. 4A) [98,99]. Continuous printing at 15 mm/s printing speed and a corresponding residence time in the static mixer of around 2.5 min was possible. Two-layer scaffolds (12 × 12 mm, 1.5 mm interstrand distance) with a grid square design-were printed as a model structure (Fig. 4B). The scaffolds were mechanically stable and presented smooth filaments of uniform thread dimensions (360 ± 34 μm diameter threads) (Fig. 4C). The microstructure of the thread surface studied by AFM (Fig. 4D) showed that NPs were uniformly distributed in the hydrogel framework and presented good integration with the hydrogel matrix, what can be attributed to the homogeneity of the bioink.

Inks without cells were formulated and printed for rheological and *in vitro* characterization of inks and printed scaffolds and are described in Sections 3.4 and 3.5.

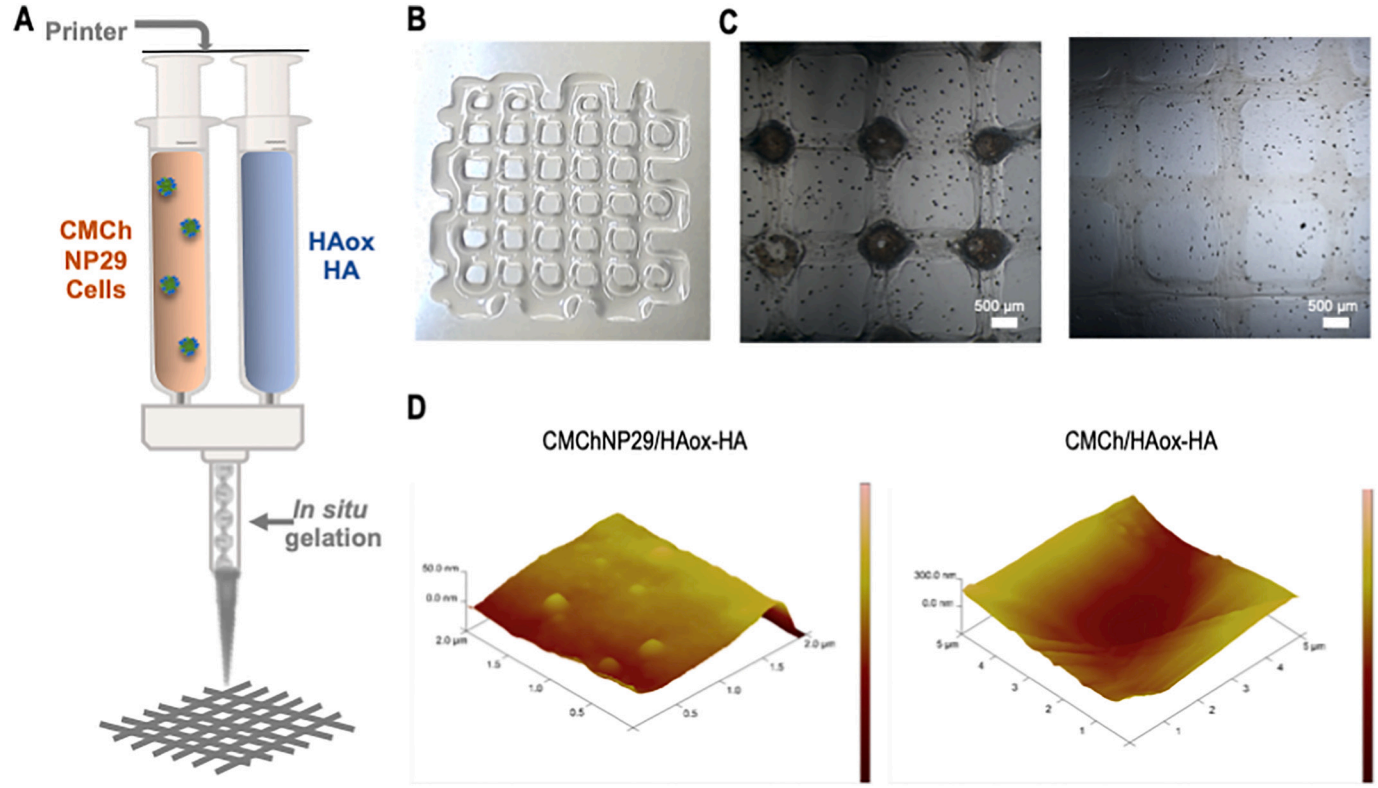

Fig. 4. (A) Schematic illustration of the bioprinting methodology. (B) Camera picture of a two-layer grid square scaffold (12 × 12 mm, 1.5 mm interstrand distance) using CMChNP29/HAox-HA formulation. (C) Light microscopy pictures of dried scaffold (left) and scaffold in PBS (right) using CMChNP29/HAox-HA formulation. (D) AFM microscopy of scaffold strand surface printed using CMChNP29/HAox-HA and CMCh/HAox-HA formulations.

3.4. Rheological properties of the ink

Time sweep experiments were performed to study the crosslinking kinetics of CMCh and HAox solutions in the presence or absence of the catechol NPs (Fig. 5A). The increase of G′ and G″ with time is associated to the formation of Schiff base linkages in the system, what lead to a crossover point of G′ and G″ that indicates the formation of a hydrogel network [104,105].A gelation time of 3.32 ± 0.53 min was observed for CMCh/NP29HAox-HA ink formulation. Gelation kinetics of this NP-loaded hydrogel was proved optimal for printing with a residence time of 2.5 min in the mixer. Gelation time obtained for CMCh/HAox-HA ink (3.65 ± 0.33 min) was in the same order of magnitude, and it was also suitable for printing. This indicates that the presence of the catechol NPs does not influence the viscosity of the bioink or impair the printing process within the conditions and geometries tested in this work.

Frequency sweep experiments with the crosslinked ink (Fig. 5B) showed that storage modulus was higher than loss modulus within 1–300 rad/s frequency range, which corroborates the formation of the hydrogel network. Frequency sweep plots with small slope were obtained for CMChNP29/HAox-HA and CMCh/HAox-HA formulations. This behavior usually correlates with weak hydrogels with shear thinning behavior [106]. The final storage modulus of NP-loaded hydrogel was slightly higher than the hydrogel without NPs. This effect can be attributed to the formation of electrostatic interactions between the NPs and the hydrogel network. However, the small difference implies that mainly the covalent crosslinking between hydrogel precursors contribute to the mechanical stability of the network. The hydrogels showed a final shear modulus G′ = 50–150 Pa at frequencies between 2 and 300 rad/s, analogous to those published for cell-laden chitosan and hyaluronic acid hydrogels in other reports [99,101,107,108]. Results correspond to soft hydrogels, suitable for soft tissue regeneration [99].

Viscosity of the ink at increasing shear rate was investigated. Both formulations, CMCh/NP29HAox-HA and CMCh/HAox-HA, presented a shear-thinning behavior right after hydrogel formation, with a linear decrease in viscosity as the shear rate increased (Fig. 5C). The shear thinning behavior is a favorable characteristic for printing since ensures that hydrogel viscosity decreases under applied deformation facilitating the flow of the material during extrusion, and it increases when deformation ceases, enabling shape fidelity of the printed features [36,109]. The viscosity of both studied solutions was relatively low compared to air pressure-based extruded inks (in the range of 30 6 × 10^7 mPa) [92,93]. The presence of the NPs and their possible interactions with the hydrogel network did not affect viscosity values. Low viscosity of the ink and the shear thinning behavior contribute to the reduction of the shear stress to which cells are exposed during extrusion, which favors cell viability [36,110–112].

3.5. 3D printed scaffolds in vitro performance

Swelling and degradation behavior of two-layer printed scaffolds of CMChNP29/HAox-HA and CMCh/HAox-HA (as control) formulations were analyzed. Fig. 6A shows that both hydrogel formulations presented similar swelling behavior in *in vitro* physiological conditions; a maximum swelling degree was obtained after 30 min of incubation (around 30%), and then swelling decreased and stabilized to reach the equilibrium state (around 5%) after 4 h. The presence of NPs in the hydrogel did not affect the swelling properties of the network. The degradation of the scaffolds was determined by monitoring the weight loss after different incubation times in physiological conditions (Fig. 6B). Both formulations presented a gradual degradation pattern with a remaining weight of about 60% within the first 6 days. However, after 28 days, degradation was relatively higher for the NPs loaded formulation (32 ± 9% of weight remaining) compared to the control (47 ± 12% of weight remaining). This effect might be attributed to the fact that the entrapped NPs establish interactions with the network influencing the degradation mechanism of the hydrogel matrix. Fig. 6C shows that scaffolds maintained their structural integrity after 28, though erosion signs can be appreciated in the optical microscopy visualization.

Swelling and biodegradability are intrinsic properties of hydrogels relevant in the wound repair process [111,113,114] and directly related to the crosslinking of the network [113,115,116]. In this case, both stability and swelling of the printed scaffolds will be influenced by the Schiff base crosslinking of the polysaccharide matrix and the treatment with $FeCl_3$ after printing, as previously demonstrated [44,117]. A moderate swelling range is observed for all scaffolds, which can be considered adequate for wound management since it can ensure a moisture environment in the wound that accelerate the re-epithelialization process [34,108,113,114]. During degradation, the release of NP29 from its scaffold may lead to slightly faster degradation in comparison to the control scaffolds without NPs. Nevertheless, the small difference between both degradation patterns indicates that presence of the NPs and their possible interactions with the hydrogel network did not significantly influence the network stability behavior. The gradual degradation of the scaffolds could match tissue regeneration rate, allowing the progressive degradation of the scaffold while the new tissues are formed, and a complete resorption is expected *in vivo* due to the presence of proteases, lipases, and other enzymes [113].

The cumulative release of the catechol NPs from the CMChNP29/HAox-HA printed scaffold was studied in simulated physiological conditions (Fig. 6D). Hydrogel films prepared using the same formulation

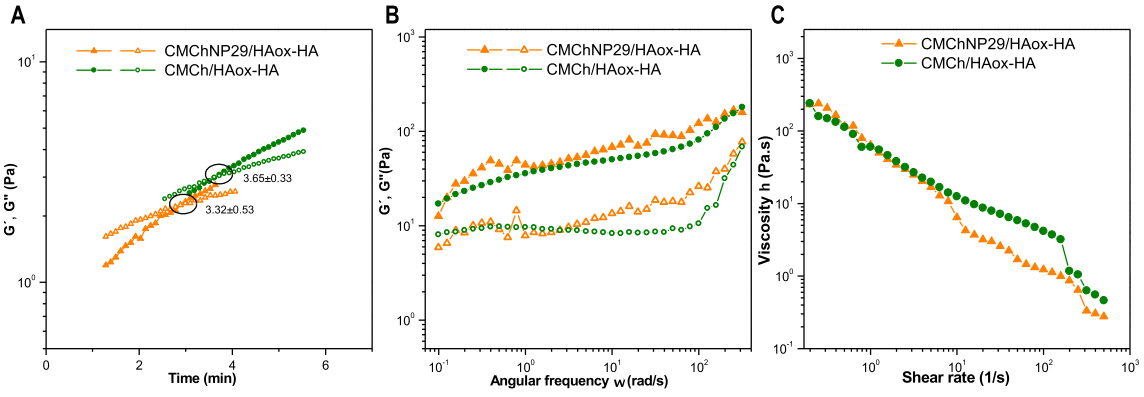

Fig. 5. Rheological curves of CMChNP29/HAox-HA bioink formulation compared to the formulation without NPs (CMCh/HAox-HA). (A) G′ (full symbols) and G″ (open symbols) moduli recorded as a function of time at a constant frequency of 1 Hz and 1% oscillatory strain. Gelation times were determined as G′and G″ crossover points. (B) G′ (full symbols) and G″ (open symbols) moduli recorded as a function of angular frequency at 1% strain. (C) Viscosity analysis of the inks as a function of shear rate.

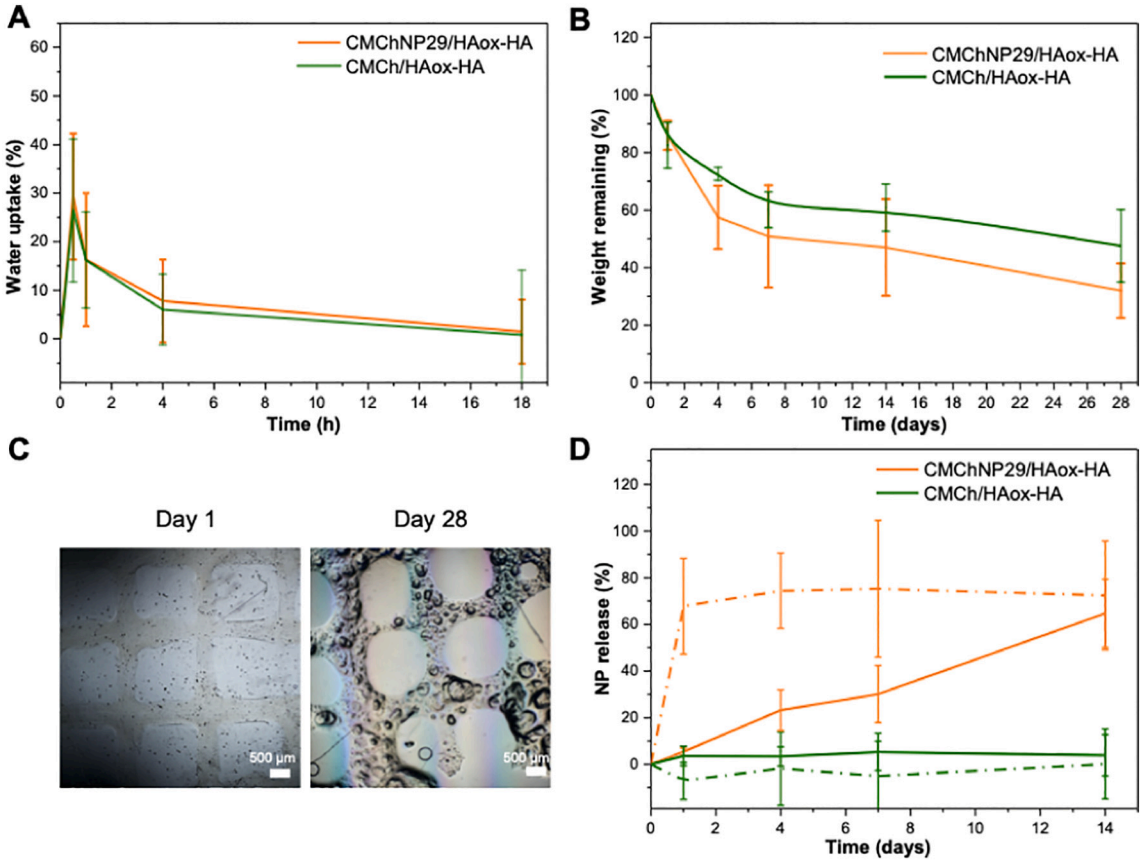

Fig. 6. (A) *In vitro* water uptake and (B) degradation profiles of CMChNP29/HAox-HA and CMCh/HAox-HA scaffolds in simulated physiological conditions. (C) Microscopic images at 2× magnification of dried scaffolds using CMChNP29/HAox-HA formulation after 1 and 28 days of incubation in PBS at 37 °C. (D) Cumulative NP29 release from hydrogel printed scaffolds (continuous lines) and films (dot lines) of similar composition as a function of time.

were also tested to compare the NPs release profile from supports with very different morphologies. A continuous release is observed of the NPs from the printed scaffolds where around 65% of the initial NPs amount was releasedafter 21 days. This behavior correlates with a zero order kinetic model presenting a sustained and slow release of the bioactive NPs. However, the release from hydrogel films was faster and not sustained; a burst release of 65% was noticed at day 1 and a plateau value of around 70% was reached after 4 days. This different release performance can be associated with the difference in the physical properties of the supports with different shapes [118]. Printed grid scaffolds allow a better entrapment of NPs and present a higher contact surface with the medium so they facilitate progressive NPs release. However, hydrogel films release the NPs located at the surface very fast, while they do not favor the release of NPs trapped inside. Obtained results suggest that NPs release rate from a printed hydrogel could be controlled by changing the 3D printed structure design, which is a very interesting feature for drug delivery strategies. Patient specific 3D printed scaffolds can offer a sustained release of the NPs to the implantation site. The controlled and localized release of the catechol functionalized NPs in the wound site is expected to provide a prolonged bioactive effect (antioxidant and anti-inflammatory) as demonstrated in section 3.2. Moreover, since NPs can serve as nanocarriers, their action could be extended to other encapsulated drugs.

3.6. Cell viability in the bioprinted scaffolds

The viability of L929 fibroblasts within the bioprinted hydrogel scaffolds was evaluated over 14 days. Fluorescence images (Fig. 7A) showed that cells were homogeneously distributed within the scaffold, indicating an effective mixing of the components in the static mixer during the extrusion process. Fig. 7B showed that cells inside the hydrogel maintained a rounded morphology, which could be due to the absence of cell adhesive sequences and the low stiffness of the hydrogel material. The nuclei staining (Fig. 7C) visualizes that the scaffolds maintained dimensional stability after 14 days of culture. Most probably it can be ascribed to the stabilization step with Fe^{3+} that provides long-term mechanical and structural integrity to the scaffolds.

Quantification of the cell viability in the bioprinted constructs after 1 day of culture (Fig. 7D) was determined from live dead assay. Results showed non-significant differences compared to the material before printing. These results suggest that shear stress produced during the bioprinting process did not have any negative effect on the short time cell viability. The viability of fibroblasts within the bioprinted scaffolds significantly increased after 7 days and remained stable until 14 days of culture, showing values between 85 and 97% respectively. High cell viability values at long times indicate that the NPs release and the polysaccharides degradation products did not negatively influence cell survival. Obtained results suggest that the bioactive properties of the catechol functionalized NPs provided a suitable environment for the encapsulated cells after bioprinting supporting long-term cell survival.

Metabolic activity of fibroblasts encapsulated into the bioprinted constructs was quantified over time using Alamar Blue assay. Results of NP-loaded bioprinted scaffolds were compared with those of bioprinted scaffolds without NPs (Fig. 7E). NP-loaded constructs supported a more stable cell growth rate than controls, showing significantly higher viability values at 4, 7 and 14 days of culture. This improved biological response was attributed to the incorporation of the catechol groups of NPs in the polysaccharide matrix. Catechol has been proposed as an activator of cell proliferation in several studies [74,89,119]. Fluorescence values for NP-loaded hydrogels after 14 days of culture were over

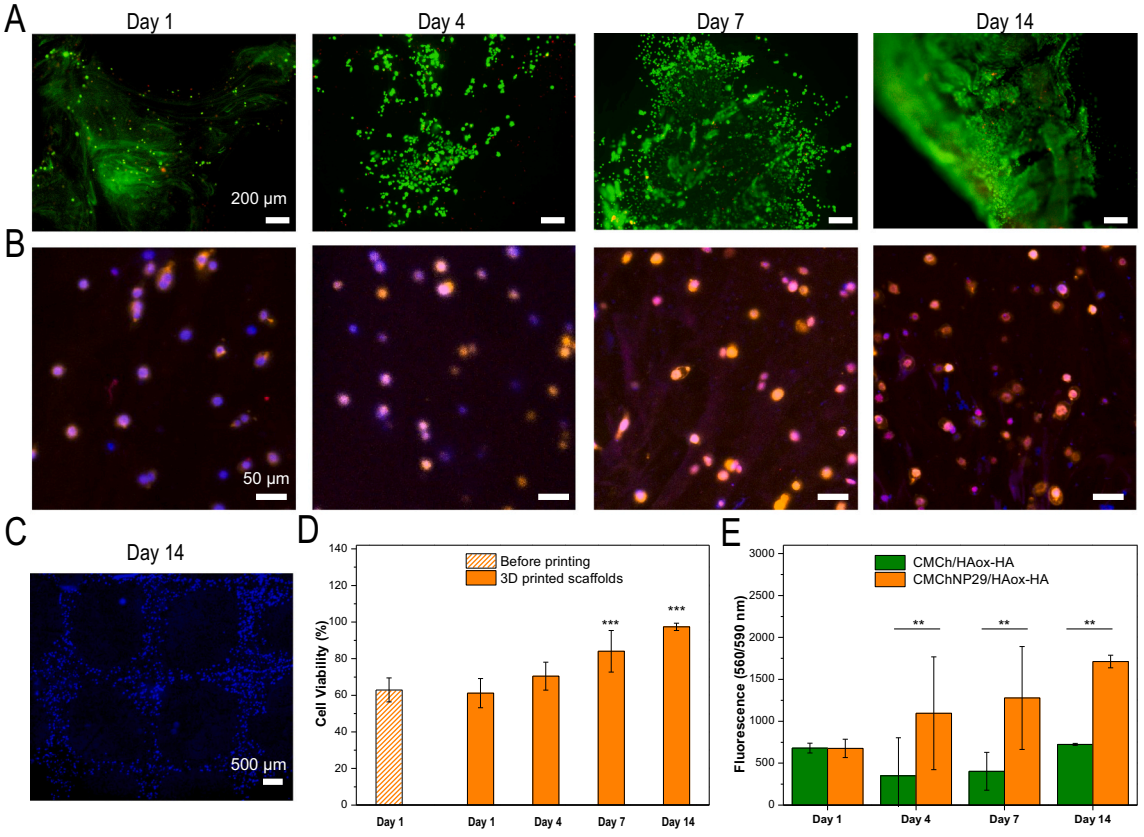

Fig. 7. (A) Fluorescence images using live dead staining and (B) confocal images of immunostaining of L929 fibroblasts embedded into CMChNP29/HAox-HA bioprinted scaffolds over 14 days of culture. (C) Fluorescence image of nuclei staining with DAPI of L929 fibroblasts in a CMChNP29/HAox-HA bioprinted scaffolds after 14 days of culture. (D) Quantification of L929 fibroblasts viability in the non-printed hydrogels at 1 day, and in the printed constructs over 14 days for CMChNP29/HAox-HA formulation. ANOVA of the results for printed scaffolds at different time points was performed in comparison with the non-printed sample at significant levels of $*p < 0.05$, $**p < 0.01$ and $***p < 0.001$. (E) Metabolic activity of L929 fibroblasts encapsulated into CMChNP29/HAox-HA and CMCh/HAox-HA bioprinted constructs quantified over time using Alamar Blue staining assay. ANOVA of the results for CMChNP29/HAox-HA sample was performed in comparison with the CMCh/HAox-HA control sample at significant levels of $*p < 0.05$, $**p < 0.01$ and $***p < 0.001$. (For interpretation of the references to colour in this figure legend, the reader is referred to the web version of this article.)

2.5-fold higher compared to the immediate values after printing of printed scaffolds with and without NPs.

Results obtained for cell studies of the developed bioprinted scaffolds are consistent with other reported systems based on chitosan or hyaluronic acid bioprinted scaffolds [120–122]. We can conclude that *in vitro* biological studies demonstrate the ability of NP-loaded hydrogel bioink to support and promote cell proliferation of encapsulated cells due to the bioactive properties of the catechol functionalized NPs, indicating that this bioink is a promising material for application in skin tissue regeneration processes.

4. Conclusions

In the present work, novel bioactive catechol functionalized nanoparticles with two different catechol contents, *i.e.* 2 and 29 M %, named NP2 and NP29 respectively, have been successfully prepared. Catechol NPs have demonstrated to serve as nanocarriers for the hydrophobic model drug coumarin-6 and possess excellent wound healing promoting activities such as: regulation of the radical oxygen species production, anti-inflammatory response, and upregulation of vascular endothelial growth factor expression. NP29 have been further integrated in a hydrogel composed of carboxymethyl chitosan and hyaluronic acid for the formulation of an advanced bioink. A reactive mixing bioprinting approach was applied to print two-layer grid square scaffolds with good mechanical stability and shape fidelity, and NPs uniformly distributed in the hydrogel framework. *In vitro* studies demonstrated the ability of the NP-loaded bioink to support cell proliferation of encapsulated fibroblasts over 14 days. The developed bioink presents properties that can be of relevance for advanced materials for wound healing therapies, including advantages such as: 1) the controlled release of the NPs in the wound site provides localized bioactive function; 2) functionalized NPs can act as nanocarriers for hydrophobic drugs; 3) printing approach used allows tailoring the geometry of the materials and formulation doses based on patient requirements for wound specific treatments.

CRediT authorship contribution statement

María Puertas-Bartolomé: Conceptualization, Methodology, Validation, Formal analysis, Investigation, Visualization Writing - original draft. **Małgorzata K.Włodarczyk-Biegun**: Formal analysis, Validation, Visualization, Writing - review & editing. **Aránzazu del Campo**: Resources, Validation, Visualization,Writing - review & editing. **Blanca Vázquez-Lasa**: Conceptualization, Investigation, Resources, Writing - review & editing, Supervision, Project administration, Funding acquisition. **Julio San Román**: Conceptualization, Investigation, Resources, Writing - review & editing, Supervision, Project administration, Funding acquisition.

Declaration of competing interest

The authors declare that they have no known competing financial interests or personal relationships that could have appeared to influence

the work reported in this paper.

Acknowledgments

Authors thank CIBER-BBN (Spain) and the Spanish Ministry of Economy and Competitivity (M. Puertas-Bartolomé scholarship BES-2015-075161) and the Spanish Ministry of Science and Innovation (PID2020-114086RB-100) for supporting this work. The authors acknowledge RegenHu company, and particularly: Sandro Figi, Dominic Ernst, Michael Kuster and Andreas Scheidegger, for the fruitful collaboration, development and providing the mixing tool. The authors thank Dr. Emmanuel Terriac from INM, Germany for assistance in the confocal imaging. B. Vázquez-Lasa is a member of the SusPlast platform from CSIC.

Appendix A. Supplementary data

Supplementary data to this article can be found online at https://doi.org/10.1016/j.msec.2021.112515.

References

[1] D. Chouhan, N. Dey, N. Bhardwaj, B.B. Mandal, Emerging and innovative approaches for wound healing and skin regeneration: current status and advances, Biomaterials 216 (2019), 119267.
[2] P. Martin, Wound healing–aiming for perfect skin regeneration, Science 276 (5309) (1997) 75–81.
[3] R.A. Clark, K. Ghosh, M.G. Tonnesen, Tissue engineering for cutaneous wounds, J. Investig. Dermatol. 127 (5) (2007) 1018–1029.
[4] A. Gosain, L.A. DiPietro, Aging and wound healing, World J. Surg. 28 (3) (2004) 321–326.
[5] D.J. Gibson, G. Schultz, Chronic wound diagnostic for matrix metalloproteinase: chronic wounds, Wound Heal. South. Afr. 2 (2) (2009) 68–70.
[6] G.S. Nyanhongo, C. Sygmund, R. Ludwig, E.N. Prasetyo, G.M. Guebitz, Synthesis of multifunctional bioresponsive polymers for the management of chronic wounds, J. Biomed. Mater. Res. B Appl. Biomater. 101 (5) (2013) 882–891.
[7] M. Berthet, Y. Gauthier, C. Lacroix, B. Verrier, C. Monge, Nanoparticle-based dressing: the future of wound treatment? Trends Biotechnol. 35 (8) (2017) 770–784.
[8] M.A.M. Jahromi, P.S. Zangabad, S.M.M. Basri, in: Nanomedicine and Advanced Technologies for Burns: Preventing Infection and Facilitating Wound Healing 123, 2018, pp. 33–64.
[9] W. Wang, K.-J. Lu, C.-H. Yu, Q.-L. Huang, Y.-ZJJon Du, in: Nano-drug Delivery Systems in Wound Treatment and Skin Regeneration 17(1), 2019, pp. 1–15.
[10] A.C. Santos, D. Rodrigues, J.A. Sequeira, Nanotechnological Breakthroughs in the Development of Topical Phytocompounds-based Formulations 572, 2019.
[11] C. He, X. Zhuang, Z. Tang, H. Tian, XJAhm Chen, in: Stimuli-sensitive Synthetic Polypeptide-based Materials for Drug and Gene Delivery 1(1), 2012, pp. 48–78.
[12] S. Kunjachan, A. Błauż, D. Möckel, in: Overcoming Cellular Multidrug Resistance Using Classical Nanomedicine Formulations 45(4), 2012, pp. 421–428.
[13] D. Sutton, N. Nasongkla, E. Blanco, JJPr Gao, in: Functionalized Micellar Systems for Cancer Targeted Drug Delivery 24(6), 2007, pp. 1029–1046.
[14] O.C. Farokhzad, RJAn Langer, in: Impact of Nanotechnology on Drug Delivery 3 (1), 2009, pp. 16–20.
[15] VPJPr Torchilin, in: Micellar Nanocarriers: Pharmaceutical Perspectives 24(1), 2007, pp. 1–16.
[16] D. Peer, J.M. Karp, S. Hong, O.C. Farokhzad, R. Margalit, RJNn Langer, in: Nanocarriers as an Emerging Platform for Cancer Therapy 2(12), 2007, pp. 751–760.
[17] S. Wu, R. Qi, H. Kuang, in: pH-responsive Drug Delivery by Amphiphilic Copolymer Through Boronate-catechol Complexation 78(2), 2013, p. 175.
[18] S. Huang, XJJoCR Fu, in: Naturally Derived Materials-based Cell and Drug Delivery Systems in Skin Regeneration 142(2), 2010, pp. 149–159.
[19] M. Puertas-Bartolomé, B. Vázquez-Lasa, Román J. San, Bioactive and bioadhesive catechol conjugated polymers for tissue regeneration, Polymers 10 (7) (2018) 768.
[20] M. Puertas-Bartolomé, M. Fernández-Gutiérrez, L. García-Fernández, B. Vázquez-Lasa, Román J. San, Biocompatible and bioadhesive low molecular weight polymers containing long-arm catechol-functionalized methacrylate, Eur. Polym. J. 98 (2018) 47–55.
[21] M. Puertas-Bartolomé, L. Benito-Garzón, S. Fung, J. Kohn, B. Vázquez-Lasa, Román J. San, Bioadhesive functional hydrogels: controlled release of catechol species with antioxidant and antiinflammatory behavior, Mater. Sci. Eng. C 105 (2019), 110040.
[22] D. Lu, H. Wang, Li Te, et al., Mussel-inspired thermoresponsive polypeptide-pluronic copolymers for versatile surgical adhesives and hemostasis, ACS Appl. Mater. Interfaces 9 (20) (2017) 16756–16766.
[23] E.Y. Jeon, B.-H. Choi, D. Jung, B.H. Hwang, H.J. Cha, Natural healing-inspired collagen-targeting surgical protein glue for accelerated scarless skin regeneration, Biomaterials 134 (2017) 154–165.
[24] L. Han, X. Lu, K. Liu, et al., Mussel-inspired adhesive and tough hydrogel based on nanoclay confined dopamine polymerization, ACS Nano 11 (3) (2017) 2561–2574.
[25] Y. Zhang, J. Zhang, M. Chen, in: A Bioadhesive Nanoparticle–Hydrogel Hybrid System for Localized Antimicrobial Drug Delivery 8(28), 2016, pp. 18367–18374.
[26] C. Pornpitchanarong, T. Rojanarata, P. Opanasopit, T. Ngawhirunpat, P.J. C. Patrojanasophon, S.B. Biointerfaces, in: Catechol-modified Chitosan/Hyaluronic Acid Nanoparticles as a New Avenue for Local Delivery of Doxorubicin to Oral Cancer Cells 196, 2020, p. 111279.
[27] J.M. Chan, J.P. Tan, A.C. Engler, in: Organocatalytic Anticancer Drug Loading of Degradable Polymeric Mixed Micelles via a Biomimetic Mechanism 49(6), 2016, pp. 2013–2021.
[28] R.J. Ono, A.L. Lee, Z.X. Voo, in: Biodegradable Strain-promoted Click Hydrogels for Encapsulation of Drug-loaded Nanoparticles and Sustained Release of Therapeutics 18(8), 2017, pp. 2277–2285.
[29] W. Gao, D. Vecchio, J. Li, in: Hydrogel Containing Nanoparticle-stabilized Liposomes for Topical Antimicrobial Delivery 8(3), 2014, pp. 2900–2907.
[30] U.F. Aly, H.A. Abou-Taleb, A.A. Abdellatif, NSJDd Tolba, in: Development, Therapy. Formulation and Evaluation of Simvastatin Polymeric Nanoparticles Loaded in Hydrogel for Optimum Wound Healing Purpose 13, 2019, p. 1567.
[31] N. Annabi, A. Tamayol, J.A. Uquillas, et al., 25th anniversary article: rational design and applications of hydrogels in regenerative medicine, Adv. Mater. 26 (1) (2014) 85–124.
[32] B.D. Ratner, S.J. Bryant, Biomaterials: where we have been and where we are going, Annu. Rev. Biomed. Eng. 6 (2004) 41–75.
[33] E. Caló, V.V. Khutoryanskiy, Biomedical applications of hydrogels: a review of patents and commercial products, Eur. Polym. J. 65 (2015) 252–267.
[34] J. Long, A.E. Etxeberria, A.V. Nand, C.R. Bunt, S. Ray, A. Seyfoddin, A 3D printed chitosan-pectin hydrogel wound dressing for lidocaine hydrochloride delivery, Mater. Sci. Eng. C 104 (2019), 109873.
[35] S.V. Murphy, A. Skardal, A. Atala, Evaluation of hydrogels for bio-printing applications, J. Biomed. Mater. Res. A 101 (1) (2013) 272–284.
[36] J. Malda, J. Visser, F.P. Melchels, et al., 25th anniversary article: engineering hydrogels for biofabrication, Adv. Mater. 25 (36) (2013) 5011–5028.
[37] M. Hospodiuk, M. Dey, D. Sosnoski, I.T. Ozbolat, The bioink: a comprehensive review on bioprintable materials, Biotechnol. Adv. 35 (2) (2017) 217–239.
[38] A. Chaudhari, K. Vig, D. Baganizi, et al., Future prospects for scaffolding methods and biomaterials in skin tissue engineering: a review, Int. J. Mol. Sci. 17 (12) (2016) 1974.
[39] A. Mora-Boza, M. Puertas-Bartolomé, B. Vázquez-Lasa, J. San Román, A. Pérez-Caballer, M. Olmeda-Lozano, Contribution of bioactive hyaluronic acid and gelatin to regenerative medicine, in: Methodologies of Gels Preparation and Advanced Applications, 2017.
[40] S.V. Kogelenberg, Z. Yue, J.N. Dinoro, C.S. Baker, G.G. Wallace, Three-dimensional printing and cell therapy for wound repair, Adv. Wound Care 7 (5) (2018) 145–156.
[41] J.M. Yang, O.S. Olanrele, X. Zhang, C.C. Hsu, Fabrication of hydrogel materials for biomedical applications, in: Novel Biomaterials for Regenerative Medicine, Springer, 2018, pp. 197–224.
[42] F. Hafezi, N. Scoutaris, D. Douroumis, J. Boateng, 3D printed chitosan dressing crosslinked with genipin for potential healing of chronic wounds, Int. J. Pharm. 560 (2019) 406–415.
[43] Z. Muwaffak, A. Goyanes, V. Clark, A.W. Basit, S.T. Hilton, S. Gaisford, Patient-specific 3D scanned and 3D printed antimicrobial polycaprolactone wound dressings, Int. J. Pharm. 527 (1–2) (2017) 161–170.
[44] M. Puertas-Bartolomé, M.K. Włodarczyk-Biegun, A. Del Campo, B. Vázquez-Lasa, J.J.P. San Román, in: 3D Printing of a Reactive Hydrogel Bio-Ink Using a Static Mixing Tool 12(9), 2020, p. 1986.
[45] R. Fort, T. Polyzoidis, Intrinsic viscosity-molecular weight relationships for poly (2-hydroxyethyl methacrylate), Eur. Polym. J. 12 (9) (1976) 685–689.
[46] H. Tan, C.R. Chu, K.A. Payne, K.G. Marra, Injectable in situ forming biodegradable chitosan–hyaluronic acid based hydrogels for cartilage tissue engineering, Biomaterials 30 (13) (2009) 2499–2506.
[47] H. Zhao, N.D. Heindel, Determination of degree of substitution of formyl groups in polyaldehyde dextran by the hydroxylamine hydrochloride method, Pharm. Res. 8 (3) (1991) 400–402.
[48] S.Y. Wang, X.Y. Lan, J.H. Xiao, J.C. Yang, Y.T. Kao, S.T. Chang, Antiinflammatory activity of Lindera erythrocarpa fruits, Phytother. Res. 22 (2) (2008) 213–216.
[49] I. Guevara, J. Iwanejko, A. Dembińska-Kieć, et al., Determination of nitrite/nitrate in human biological material by the simple griess reaction, Clin. Chim. Acta 274 (2) (1998) 177–188.
[50] M.S. Choi, S.H. Lee, H.S. Cho, et al., Inhibitory effect of obovatol on nitric oxide production and activation of NF-κB/MAP kinases in lipopolysaccharide-treated RAW 264.7 cells, Eur. J. Pharmacol. 556 (1–3) (2007) 181–189.
[51] J.F. Jansen, E.E. Houben, P.H. Tummers, D. Wienke, J. Hoffmann, Real-time infrared determination of photoinitiated copolymerization reactivity ratios: application of the hilbert transform and critical evaluation of data analysis techniques, Macromolecules 37 (6) (2004) 2275–2286.
[52] T. Chen, Y. Chen, H.U. Rehman, et al., Ultratough, self-healing, and tissue-adhesive hydrogel for wound dressing, ACS Appl. Mater. Interfaces 10 (39) (2018) 33523–33531.

[53] C.E. Brubaker, H. Kissler, L.-J. Wang, D.B. Kaufman, P.B. Messersmith, Biological performance of mussel-inspired adhesive in extrahepatic islet transplantation, Biomaterials 31 (3) (2010) 420–427.
[54] U. Hasegawa, M. Moriyama, H. Uyama, A.J. van der Vlies, Catechol-bearing block copolymer micelles: structural characterization and antioxidant activity, Polymer 66 (2015) 1–7.
[55] J. Yang, M.A.C. Stuart, M. Kamperman, Jack of all trades: versatile catechol crosslinking mechanisms, Chem. Soc. Rev. 43 (24) (2014) 8271–8298.
[56] I. Rivolta, A. Panariti, B. Lettiero, et al., Cellular uptake of coumarin-6 as a model drug loaded in solid lipid nanoparticles, J. Physiol. Pharmacol. 62 (1) (2011) 45.
[57] J.P.K. Tan, Z.X. Voo, S. Lim, et al., Effective encapsulation of apomorphine into biodegradable polymeric nanoparticles through a reversible chemical bond for delivery across the blood–brain barrier, Nanomedicine 17 (2019) 236–245.
[58] P. Shende, HJLs Gupta, in: Formulation and Comparative Characterization of Nanoparticles of Curcumin Using Natural, Synthetic and Semi-synthetic Polymers for Wound Healing 253, 2020, p. 117588.
[59] V.L.R. Correa, J.A. Martins, T.R. de Souza, in: Melatonin Loaded Lecithin-chitosan Nanoparticles Improved the Wound Healing in Diabetic Rats 162, 2020, pp. 1465–1475.
[60] M. Malmsten, Antimicrobial and antiviral hydrogels, Soft Matter 7 (19) (2011) 8725–8736.
[61] R. Zeng, C. Lin, Z. Lin, et al., Approaches to cutaneous wound healing: basics and future directions, Cell Tissue Res. 374 (2) (2018) 217–232.
[62] R. Palao-Suay, M.R. Aguilar, F.J. Parra-Ruiz, et al., Anticancer and antiangiogenic activity of surfactant-free nanoparticles based on self-assembled polymeric derivatives of vitamin E: Structure–activity relationship, Biomacromolecules 16 (5) (2015) 1566–1581.
[63] E. Nagababu, J.M. Rifkind, S. Boindala, L. Nakka, Assessment of antioxidant activity of eugenol in vitro and in vivo, in: Free Radicals and Antioxidant Protocols, Springer, 2010, pp. 165–180.
[64] D. Huber, A. Grzelak, M. Baumann, et al., Anti-inflammatory and anti-oxidant properties of laccase-synthesized phenolic- O -carboxymethyl chitosan hydrogels, New Biotechnol. 40 (2018) 236–244.
[65] N. Schweigert, A.J. Zehnder, R.I. Eggen, Chemical properties of catechols and their molecular modes of toxic action in cells, from microorganisms to mammals, Environ. Microbiol. 3 (2) (2001) 81–91.
[66] Y. Cai, Q. Luo, M. Sun, H. Corke, Antioxidant activity and phenolic compounds of 112 traditional chinese medicinal plants associated with anticancer, Life Sci. 74 (17) (2004) 2157–2184.
[67] L. He, T. He, S. Farrar, L. Ji, T. Liu, X. Ma, Antioxidants maintain cellular redox homeostasis by elimination of reactive oxygen species, Cell. Physiol. Biochem. 44 (2) (2017) 532–553.
[68] İ. Gülçin, Antioxidant activity of caffeic acid (3, 4-dihydroxycinnamic acid), Toxicology 217 (2–3) (2006) 213–220.
[69] T. Bjarnsholt, K. Kirketerp-Møller, P.Ø. Jensen, et al., Why chronic wounds will not heal: a novel hypothesis, Wound Repair Regen. 16 (1) (2008) 2–10.
[70] E. Novo, M. Parola, Redox mechanisms in hepatic chronic wound healing and fibrogenesis, Fibrogenesis Tissue Repair 1 (1) (2008) 5.
[71] S.A. Eming, T. Krieg, J.M. Davidson, Inflammation in wound repair: molecular and cellular mechanisms, J. Investig. Dermatol. 127 (3) (2007) 514–525.
[72] H. Brem, O. Stojadinovic, R.F. Diegelmann, et al., Molecular markers in patients with chronic wounds to guide surgical debridement, Mol. Med. 13 (1–2) (2007) 30.
[73] T.E. Cawston, A.J. Wilson, Understanding the role of tissue degrading enzymes and their inhibitors in development and disease, Best Pract. Res. Clin. Rheumatol. 20 (5) (2006) 983–1002.
[74] W. Chen, X. Shen, Y. Hu, et al., Surface functionalization of titanium implants with chitosan-catechol conjugate for suppression of ROS-induced cells damage and improvement of osteogenesis, Biomaterials 114 (2017) 82–96.
[75] M. Kojima, T. Morisaki, K. Izuhara, et al., Lipopolysaccharide increases cyclo-oxygenase-2 expression in a colon carcinoma cell line through nuclear factor-κB activation, Oncogene 19 (9) (2000) 1225.
[76] K.V. Dileep, I. Tintu, P.K. Mandal, P. Karthe, M. Haridas, C. Sadasivan, Binding to PLA2 may contribute to the anti-inflammatory activity of catechol, Chem. Biol. Drug Des. 79 (1) (2012) 143–147.
[77] L.T. Zheng, G.-M. Ryu, B.-M. Kwon, W.-H. Lee, K. Suk, Anti-inflammatory effects of catechols in lipopolysaccharide-stimulated microglia cells: inhibition of microglial neurotoxicity, Eur. J. Pharmacol. 588 (1) (2008) 106–113.
[78] M. Larrosa, C. Luceri, E. Vivoli, et al., Polyphenol metabolites from colonic microbiota exert anti-inflammatory activity on different inflammation models, Mol. Nutr. Food Res. 53 (8) (2009) 1044–1054.
[79] J. Huang, T. de Paulis, J.M. May, Antioxidant effects of dihydrocaffeic acid in human EA. hy926 endothelial cells, J. Nutr. Biochem. 15 (12) (2004) 722–729.
[80] A. Francesko, D.S. da Costa, P. Lisboa, R.L. Reis, I. Pashkuleva, T. Tzanov, GAGs-thiolated chitosan assemblies for chronic wounds treatment: control of enzyme activity and cell attachment, J. Mater. Chem. 22 (37) (2012) 19438–19446.
[81] G. Mohammad, H. Pandey, K. Tripathib, Diabetic wound healing and its angiogenesis with special reference to nanoparticles, Dig. J. Nanomater. Biostruct. 3 (2008) 203–208.
[82] A. Mohandas, B. Anisha, K. Chennazhi, R. Jayakumar, Chitosan–hyaluronic acid/VEGF loaded fibrin nanoparticles composite sponges for enhancing angiogenesis in wounds, Colloids Surf. B: Biointerfaces 127 (2015) 105–113.
[83] S.T. Nillesen, P.J. Geutjes, R. Wismans, J. Schalkwijk, W.F. Daamen, T.H. van Kuppevelt, Increased angiogenesis and blood vessel maturation in acellular collagen–heparin scaffolds containing both FGF2 and VEGF, Biomaterials 28 (6) (2007) 1123–1131.
[84] P. Carmeliet, Angiogenesis in life, disease and medicine, Nature 438 (7070) (2005) 932–936.
[85] Z. Mao, H. Shi, R. Guo, et al., Enhanced angiogenesis of porous collagen scaffolds by incorporation of TMC/DNA complexes encoding vascular endothelial growth factor, Acta Biomater. 5 (8) (2009) 2983–2994.
[86] L. Elviri, A. Bianchera, C. Bergonzi, R. Bettini, Controlled local drug delivery strategies from chitosan hydrogels for wound healing, Expert Opin. Drug Deliv. 14 (7) (2017) 897–908.
[87] N. Ferrara, H.-P. Gerber, J. LeCouter, The biology of VEGF and its receptors, Nat. Med. 9 (6) (2003) 669–676.
[88] Y.M. Elçin, V. Dixit, G. Gitnick, Extensive in vivo angiogenesis following controlled release of human vascular endothelial cell growth factor: implications for tissue engineering and wound healing, Artif. Organs 25 (7) (2001) 558–565.
[89] J. Shin, J.S. Lee, C. Lee, et al., Tissue adhesive catechol-modified hyaluronic acid hydrogel for effective, minimally invasive cell therapy, Adv. Funct. Mater. 25 (25) (2015) 3814–3824.
[90] H.-J. Park, Y. Jin, J. Shin, et al., Catechol-functionalized hyaluronic acid hydrogels enhance angiogenesis and osteogenesis of human adipose-derived stem cells in critical tissue defects, Biomacromolecules 17 (6) (2016) 1939–1948.
[91] M. Xu, A. Khan, T. Wang, et al., Mussel-inspired hydrogel with potent in vivo contact-active antimicrobial and wound healing promoting activities, ACS Appl. Bio Mater. 2 (8) (2019) 3329–3340.
[92] S. Derakhshanfar, R. Mbeleck, K. Xu, X. Zhang, W. Zhong, M. Xing, 3D bioprinting for biomedical devices and tissue engineering: a review of recent trends and advances, Bioact. Mater. 3 (2) (2018) 144–156.
[93] H. Cui, M. Nowicki, J.P. Fisher, L.G. Zhang, 3D bioprinting for organ regeneration, Adv. Healthc. Mater. 6 (1) (2017) 1601118.
[94] M.K. Włodarczyk-Biegun, A. del Campo, 3D bioprinting of structural proteins, Biomaterials 134 (2017) 180–201.
[95] C. Intini, L. Elviri, J. Cabral, et al., 3D-printed chitosan-based scaffolds: an in vitro study of human skin cell growth and an in-vivo wound healing evaluation in experimental diabetes in rats, Carbohydr. Polym. 199 (2018) 593–602.
[96] K. Ye, R. Felimban, K. Traianedes, et al., Chondrogenesis of infrapatellar fat pad derived adipose stem cells in 3D printed chitosan scaffold, PLoS One 9 (6) (2014).
[97] Q. Wu, D. Therriault, M.-C. Heuzey, Processing and properties of chitosan Inks for 3D printing of hydrogel microstructures, ACS Biomater Sci. Eng. 4 (7) (2018) 2643–2652.
[98] T. Hozumi, S. Ohta, T. Ito, Analysis of the calcium alginate gelation process using a kenics static mixer, Ind. Eng. Chem. Res. 54 (7) (2015) 2099–2107.
[99] K. Bootsma, M.M. Fitzgerald, B. Free, et al., 3D printing of an interpenetrating network hydrogel material with tunable viscoelastic properties, J. Mech. Behav. Biomed. Mater. 70 (2017) 84–94.
[100] N.T.-P. Nguyen, L.V.-H. Nguyen, N.M.-P. Tran, T.-H. Nguyen, C.-K. Huynh, T. V. Van, Synthesis of cross-linking chitosan-hyaluronic acid based hydrogels for tissue engineering applications, in: Paper Presented at: International Conference on the Development of Biomedical Engineering in Vietnam, 2017.
[101] L. Song, L. Li, T. He, Peritoneal adhesion prevention with a biodegradable and injectable N,O-carboxymethyl chitosan-aldehyde hyaluronic acid hydrogel in a rat repeated-injury model, Sci. Rep. 6 (Nov 21 2016) 37600.
[102] S. Khorshidi, A. Karkhaneh, A self-crosslinking tri-component hydrogel based on functionalized polysaccharides and gelatin for tissue engineering applications, Mater. Lett. 164 (2016) 468–471.
[103] A.L.R. Mercê, L.C.M. Carrera, L.K.S. Romanholi, MaÁL Recio, Aqueous and solid complexes of iron (III) with hyaluronic acid: potentiometric titrations and infrared spectroscopy studies, J. Inorg. Biochem. 89 (3-4) (2002) 212–218.
[104] L. Weng, X. Chen, W. Chen, Rheological characterization of in situ crosslinkable hydrogels formulated from oxidized dextran and N-carboxyethyl chitosan, Biomacromolecules 8 (4) (2007) 1109–1115.
[105] N.T.-P. Nguyen, L.V.-H. Nguyen, N.M.-P. Tran, et al., The effect of oxidation degree and volume ratio of components on properties and applications of in situ cross-linking hydrogels based on chitosan and hyaluronic acid, Mater. Sci. Eng. C 103 (109670) (2019).
[106] S.-H. Hsiao, S.-h. Hsu, Synthesis and characterization of dual stimuli-sensitive biodegradable polyurethane soft hydrogels for 3D cell-laden bioprinting, ACS Appl. Mater. Interfaces 10 (35) (2018) 29273–29287.
[107] L. Li, N. Wang, X. Jin, et al., Biodegradable and injectable in situ cross-linking chitosan-hyaluronic acid based hydrogels for postoperative adhesion prevention, Biomaterials 35 (12) (2014) 3903–3917.
[108] Y. Deng, J. Ren, G. Chen, et al., Injectable in situ cross-linking chitosan-hyaluronic acid based hydrogels for abdominal tissue regeneration, Sci. Rep. 7 (1) (2017) 2699.
[109] T. Jungst, W. Smolan, K. Schacht, T. Scheibel, Groll Jr, Strategies and molecular design criteria for 3D printable hydrogels, Chem. Rev. 116 (3) (2016) 1496–1539.
[110] B.A. Aguado, W. Mulyasasmita, J. Su, K.J. Lampe, S.C. Heilshorn, Improving viability of stem cells during syringe needle flow through the design of hydrogel cell carriers, Tissue Eng. A 18 (7–8) (2011) 806–815.
[111] K. Hölzl, S. Lin, L. Tytgat, S. Van Vlierberghe, L. Gu, A. Ovsianikov, Bioink properties before, during and after 3D bioprinting, Biofabrication 8 (3) (2016), 032002.
[112] K. Nair, M. Gandhi, S. Khalil, et al., Characterization of cell viability during bioprinting processes, Biotechnol. J. 4 (8) (2009) 1168–1177.
[113] D. Huber, A. Grzelak, M. Baumann, et al., Anti-inflammatory and anti-oxidant properties of laccase-synthesized phenolic-O-carboxymethyl chitosan hydrogels, New Biotechnol. 40 (2018) 236–244.
[114] S.R. Caliari, J.A. Burdick, A practical guide to hydrogels for cell culture, Nat. Methods 13 (5) (2016) 405.

[115] X. Peng, Y. Peng, B. Han, W. Liu, F. Zhang, R.J. Linhardt, IO_4^-stimulated crosslinking of catechol-conjugated hydroxyethylchitosan as a tissue adhesive, J. Biomed. Mater. Res. B Appl. Biomater. (2018).
[116] R. Barbucci, A. Magnani, M. Consumi, Swelling behavior of carboxymethylcellulose hydrogels in relation to cross-linking, pH, and charge density, Macromolecules 33 (20) (2000) 7475–7480.
[117] Y. Xin, J. Yuan, Schiff's base as a stimuli-responsive linker in polymer chemistry, Polym. Chem. 3 (11) (2012) 3045–3055.
[118] J. Yan, Y. Wang, X. Zhang, et al., Snakegourd root/Astragalus polysaccharide hydrogel preparation and application in 3D printing, Int. J. Biol. Macromol. 121 (2019) 309–316.
[119] A.I. Neto, A.C. Cibrão, C.R. Correia, et al., Nanostructured polymeric coatings based on chitosan and dopamine-modified hyaluronic acid for biomedical applications, Small 10 (12) (2014) 2459–2469.
[120] A.R. Akkineni, T. Ahlfeld, A. Lode, M. Gelinsky, A versatile method for combining different biopolymers in a core/shell fashion by 3D plotting to achieve mechanically robust constructs, Biofabrication 8 (4) (2016), 045001.
[121] Q. Gu, E. Tomaskovic-Crook, R. Lozano, et al., Functional 3D neural mini-tissues from printed gel-based bioink and human neural stem cells, Adv. Healthc. Mater. 5 (12) (2016) 1429–1438.
[122] I. Noh, N. Kim, H.N. Tran, J. Lee, C. Lee, 3D printable hyaluronic acid-based hydrogel for its potential application as a bioink in tissue engineering, Biomater. Res. 23 (1) (2019) 3.